Pontificia Universidad Católica del Perú

Escuela de Posgrado

Tesis de Maestría

Theoretical and numerical investigations of the parametric resonance of the mechanical vibrissa

Autor:

Cesar Auguto Perez Tineo

Tesis para optar el grado académico de

Magíster en Ingeniería Mecánica

Asesor (PUCP): Prof. Dipl.-Ing. Jorge Hernan Alencastre Miranda

Tutor Responsable (TU Ilmenau): Dr. Tatiana Volkova/ M.Sc.Christoph Will

Profesor Responsable (TU Ilmenau): Prof. Dr.-Ing. Habil. K. Zimmerman

Presidente de Jurado (PUCP): Prof. Dipl.-Ing. Eliseo Benjamin Barriga Gamarra

Jurado (PUCP): Prof. Dipl.-Ing. Jorge Antonio Rodriguez Hernandez

Fecha y Lugar:

31/03/2016

Lima-Perú

TECHNISCHE UNIVERSITÄT
ILMENAU

Fakultät für Maschinenbau

Fachgebiet Technische Mechanik

Aufgabenstellung für die Master-Arbeit

Von Cesar Augusto Perez Tineo

Thema: Theoretische und numerische Untersuchungen der parametrischen Resonanz mechanischer Vibrissen

Im Rahmen des Projektes "Technische, nicht-visuelle Charakterisierung von Substratkontakten nach dem biologischen Vorbild carpaler Vibrissen" werden biologisch-inspirierte mechanische Sensorsysteme entwickelt. Vibrissen sind Tasthaare von Säugetieren. Die Wechselwirkungen mit der Objektoberfläche führen zu Schwingungen der Vibrisse, die durch die Rezeptoren im Follikel-Sinus-Komplex erkannt, kodiert und nach einer Signalübertragung im Gehirn verarbeitet werden.

Ziel dieser Arbeit ist es, eine theoretische Basis für die Resonanz-Hypothese der Vibrissen während des Tastprozesses zu erarbeiten unter Verwendung analytischer und numerischer Methoden. Die Arbeit gliedert sich in folgende Teilaufgaben:

- Kurze Darstellung der Vibrissenanatomie und des Standes der Technik
- Entwicklung eines mechanischen Modells der Vibrisse mit konstanter Krümmung auf Basis der Euler-Bernoulli-Theorie
- Numerische Berechnung der Schwingungen des Balkens mit Hilfe der FEM-Methode für verschiedene Erregungsfrequenzen
- Erweiterung des Modells durch Berücksichtigung der variablen Krümmung und der Verjüngung des Querschnitts
- Vergleich von numerischen und analytischen Ergebnissen und Diskussion
- Optional: Erstellung eines experimentellen Aufbaus und Messungen
- Mündliche Abschlusspräsentation und schriftliche Dokumentation

Ausgabedatum:	01.09.2015
Verantwortlicher Hochschullehrer:	Univ.-Prof. Dr.-Ing. habil. K. Zimmermann
Betreuer an der TU Ilmenau:	Dr. Tatiana Volkova
	M.Sc. Christoph Will

Ilmenau, 1.9.2015
Ort, Datum

K. Zimmermann
Unterschrift des verantwortlichen Hochschullehrers

Ilmenau, 1.9.2015
Ort, Datum

Unterschrift des Studierenden

I Declaration

Hereby, I declare that I have elaborated the present work without any non-specified assistance. The people involved in the research, literature, as well as any other resource used in this thesis, has been completely specified throughout and at the end of the text.

29st February 2016, Ilmenau

Signature _____

II Abstract

In nature, vibrissae are tactile hairs of mammals used as sensor elements for the exploring the surrounding area. These hairs, also known as whiskers, can be found in different locations on an animals body. Mystacial vibrissae are distributed over a whiskerpad on a muzzle. Carpal vibrissae are located on the downside aspect of the forelimbs of mammals. The vibrissal hair has a conical shape and grows from a special heavily innervated hair follicle incorporating a capsule of blood. As the hair itself has no receptors along its length, the vibrissa may be considered as a system for transmitting forces and torques that arise from the contact between the hair and an object to sensory receptors inside the follicle.

The present thesis deals with the vibrational motion of vibrissae during natural exploratory behaviour from the mechanical point of view. The phenomenon of the parametric resonance of the vibrissa is investigated theoretically and numerically. In the first part of this thesis, two mechanical models of an elastic beam are presented based on findings in the literature. The first model considers a straight beam with the linearly decreasing radius of the circular cross-section. The second model takes into account the circular natural configuration of the cylindrical beam. Within these models, the small transverse vibration of the beam under a periodic following force at the tip are analysed using the Euler-Bernoulli beam theory and asymptotic methods of mechanics.

In the second part of the thesis, the numerical analysis of the problems is performed based on the finite element method using ANSYS 16.2 software. For each model, the dynamical response of the system on the parametric excitation is simulated for different frequency values.

It is shown theoretically and numerically that at specific ranges of the excitation frequency the phenomenon of the parametric resonance of the beam takes place. That means that the amplitude of vibrations of the beam increases exponentially with time, when it is stimulated within one of the frequency ranges of the parametric resonance. These ranges depend on the geometrical and material parameters of the beam model, as well as the amplitude of the periodic excitation.

III Kurzzusammenfassung

Tasthaare von Säugetieren werden als Vibrissen oder Schnurrhaare bezeichnet. Sie dienen der Erkundung der Umgebung und befinden sich an verschiedenen Stellen des Tierkörpers. Mystaziale Vibrissen sind im Bereich der Schnauze zu finden. Karpale Vibrissen befinden sich an der Unterseite der Vordergliedmaen von Säugetieren. Das Vibrissenhaar hat eine konische Form und wächst aus einem speziellen, stark innervierten Haarfollikel, der in einem Blutsinus eingegliedert ist. Da das Haar selbst keine Rezeptoren hat, kann es als ein bertragungssystem für Kräfte und Momente zum Rezeptorsystem im Follikel betrachtet werden. Kräfte und Momente entstehen aus dem Kontakt des Haars zu einem Objekt.

In der vorliegenden Masterarbeit wird die Schwingung der Vibrisse während eines natürlichen Erkundungsprozesses aus dem Blickwinkel der Mechanik untersucht. Das Phänomen der parametrischen Resonanz der Vibrisse wird analytisch und numerisch betrachtet. Im ersten Teil der Arbeit werden zwei Modelle eines elastischen Balkens aus der Literatur verwendet. Das erste Modell besteht aus einem geraden Balken mit einer kreisrunden Querschnittsfläche mit linear abnehmenden Radius. Im zweiten Modell wird die natürliche Krümmung der Vibrisse in Form eines zylindrischen Balkens mit kreisbogenförmiger Stabachse berücksichtigt. Unter Verwendung der Euler-Bernoulli-Balkentheorie und asymptotischen Methoden der Mechanik werden kleine transversale Schwingungen des Balkens analysiert. Sie werden am Stabende durch eine periodische, der Verformung folgenden Kraft ausgelöst.

Im zweiten Teil der Arbeit folgt die numerische Analyse des Problems mit Hilfe der Finiten Elemente Methode. Verwendet wird das Programmpaket ANSYS 16.2. Für jedes Modell wird die dynamische Antwort der parametrischen Erregung für verschiedene Frequenzwerte simuliert.

Es wird analytisch und numerisch gezeigt, dass für spezifische Wertebereiche der Erregungsfrequenz das Phänomen der parametrischen Resonanz des Balkens entsteht. Das heit, die Schwingungsamplitude des Balkens wächst über die Zeit exponentiell an, wenn es mit einer Frequenz aus dem Bereich der parametrischen Resonanz erregt wird. Dieser Bereich ist abhängig von geometrischen Parametern, Materialeigenschaften und von der Amplitude der periodischen Erregung.

IV Acknowledgment

I would like to express my gratitude to Univ.-Prof. Dr.-Ing. habil. Klaus Zimmermann, for giving me the opportunity of the theme of the present thesis , it has meant to deepen my knowledge obtained during the study of this master science.

My sincere thanks also goes to Dr.-Ing. Valter Böhm, for his help and support during of the develop of the thesis.

I would like to express my gratitude to my supervisor, M.Sc. Christoph Will, whose expertise, understanding, and patience, added considerably to my graduate experience.

A very special thanks goes out to Dr. Tatiana Volkova, for the motivation and encouragement. She provided me with direction, technical support. It was though her, persistence, understanding and patience. I doubt that I will ever be able to convey my appreciation fully, but I owe him my eternal gratitude.

I would also like to express my gratitude to Univ.-Prof. Dipl.-Ing. Jorge Alencastre, for his support as thesis supervisor.

I would also like to thank my family for the support they provided me through my entire life and in particular, I must acknowledge my wife, Mary.

Finally, I would like to thank to my friends, who since the beginning of the study and particularly in last months, always supported and motivated me.

V Symbols and Abbreviations

A	Cross-section area
a	Amplitude
a_0	Averaged amplitude
c	Stiffness of the spring
d	Diameter of the beam
E	Youngs modulus
$\dot{e}_x$, $\dot{e}_y$, $\dot{e}_z$	Cartesian basic vectors
$\dot{F}(t)$	Periodic force
F_0	Amplitude of the force $\dot{F}(t)$
$f(t)$	Displacement function
G	Shear modulus
g	Gravitational acceleration
I_z	Moment of inertia of a cross-section
k	Timoshenko shear coefficient
L	Length of the beam
l	Length of the pendulum
$\dot{M}_{bz}$	Bending moment
m	Mass of a system
m_0	Mass of the beam's element
$\dot{N}$	Normal force
$\dot{n}_t$	Normal to the cross-section at the tip
$\dot{Q}_y$	Transverse shear force
q	external load
R_0	Radius of the arc
$R(\omega_0)$	Rayleigh's quotient
r_b	Radius of the beam at the base
r_t	Radius of the beam at the tip
s	Natural length parameter
t	Time
t_c	Characteristic time
v	Transverse displacement
x, y, z	Cartesian coordinates
β	Eigenvalue parameter
γ	Dimensionless excitation frequency

$\gamma(x, t)$	Shear angle
δ	Radius ratio
ε	Dimensionless parameter
$\theta(t)$	Angular displacement
$\theta(x, t)$	Angle of rotation of the beam axis
κ_0	Curvature of the beam
λ	Eigenvalue
ν	Ordinary frequency (in Hz)
ρ	Density
τ	Dimensionless time
φ	Phase angle
ϕ	Angle of the arc
Ω	Angular excitation frequency
ω	Angular frequency
ω_0	Natural vibration frequency

DOF	Degree of freedom
FEM	Finite element method
FSC	Follicle-sinus complex
CCB	Circular cylindrical beam
MPC	Multi-point constraint bonded contact
PDE	Partial differential equation
SCB	Straight cylindrical beam
TCB	Truncated conical beam

Contents

1 Introduction and motivation

Vibrissae are tactile hairs of mammals used as sensor elements for the exploring the surrounding area. These hairs, also known as whiskers, can be found in different locations on an animals body. Mystacial vibrissae, for example, are distributed over a whiskerpad on a muzzle and well organized in rows and columns. Carpal vibrissae are located on the downside aspect of the forelimbs of mammals. The vibrissal hair has a conical shape and grows from a special heavily innervated hair follicle incorporating a capsule of blood, called follicle-sinus complex. As the hair itself has no receptors along its length, the vibrissa may be considered as a system for transmitting forces and torques that arise from the contact between the hair and an object to sensory receptors inside the follicle. This information is then sent by nerves to the brain.

Scientists, biologists and engineers would like to understand the functional principles of the vibrissal sensing system from different aspects. Neuroscientists would like to figure out how nerve impulses from vibrissae are processed to the brain and how an animal encodes the information. They perform laboratory experiments with living creatures. Biologists usually describe the anatomy and morphology of vibrissae from species to species. They believe that the vibrissal sensing system played an important role during evolutionary development of mammals. For the engineers, the biological vibrissa gives an inspiration to design various artificial tactile sensors and find possible applications for them.

The present thesis deals with the vibrational motion of vibrissae during natural exploratory behaviour of mammals. It may be seen as a part of the scientific research within the project "Technische, nicht-visuelle Charakterisierung von Substratkontakten nach dem biologischen Vorbild carpaler Vibrissen".

In this work, the phenomenon of the parametric resonance of the vibrissa is considered from the mechanical point of view. The main aim is to present numerical investigations that should provide a basis for the theoretical studies produced in the project.

The thesis starts with the brief introduction of the biological paradigm of vibrissae. The Chapter 2 gives a short overview of the current state of the art in characterization and modelling of vibrissae.

In Chapter 3, the resonance phenomenon in forced and parametrically excited vibrations is described by giving examples of simple mechanical sys-

tems.

In Chapters 4 and 5 of the thesis, two theoretical models of an elastic beam under an parametric excitation are presented. They take into account variable radius of the cross-section and natural configuration of the beam/vibrissa.

The Chapters 6 presents the results of numerical simulations of considered problems that are performed based on the finite element method.

Finally, general conclusions of the work are drawn in Chapter 7.

Appendix A contains the report preview of the simulation in ANSYS 16.2 Workbench.

2 The biological paradigm

2.1 Vibrissae — tactile biological sensors

Vibrissae are specialized tactile sensor hairs. In nature, these hairs, also known as whiskers, can be found in different locations on a mammals body. Mystacial vibrissae are distributed over a whiskerpad on a muzzle and well organized in rows and columns. Carpal vibrissae are located on the downside aspect of the forelimbs of mammals (Fig. 2.1). Each vibrissa is embedded in and supported by its own special heavily innervated hair follicle, called follicle-sinus complex (FSC). Vibrissae are sometime called sinus hairs, because the FSC contains a circular blood sinus, which ensures the viscolelastic foundation of the vibrissal hair (Fig. 2.2).

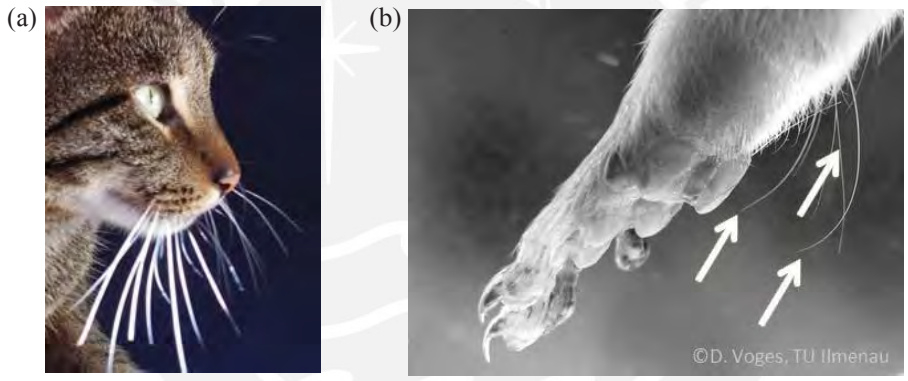

Figure 2.1: Vibrissae in mammals: a) Mystacial pad of vibrissae of a house cat [1]; b) Triple of carpal vibrissae at a forelimb of *Rattus norvegicus* [2]

There results of experimental measurements of the vibrissa diameter at different locations indicate that the diameter decreases linearly along the length [3, 4]. Figure 2.3 shows cross-sections of a macro vibrissa at the base. A hollow medulla is observed from the base to approximately half of the overall length, which is then partially filled by compact tissue, until it disappears completely near the tip [4].

According to [3], the vibrissae can be approximately as a thin, conical (tapered) rod, with a length up to 10 mm, and the diameter decreases linearly from the base to the tip between 0.1 mm to 0.001 mm. It is shown that approximately 60-70% of the vibrissae are planar and their shape can be

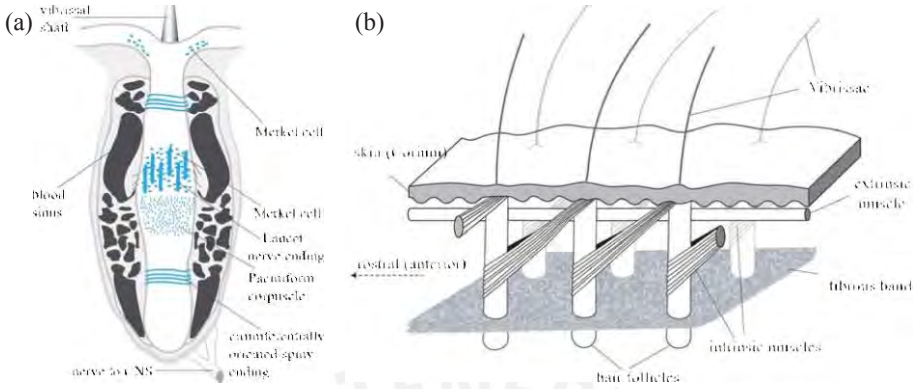

Figure 2.2: a) The FSC of a vibrissa [1]; b) Schematic drawing of neighboring mystacial follicles [5, 6]

approximated by a parabola [7]. In [8], the variation in Young's modulus along the length of a rat vibrissa is observed experimentally. The averaged value of Young's modulus for tip segments is reported to be larger than for base segments: 3.96 ± 1.60 Gpa and 2.90 ± 1.25Gpa, respectively.

2.2 Functional role of vibrissae

The functional role of vibrissae vary from animal to animal and is best developed in rodents, especially rats, squirrels and mice. These tactile hairs are particularly important for navigation, detection of objects and texture discrimination during natural exploratory behaviour of mammals. Vibrissae provide an anaimal with information about spatial existing boundaries in the environment. In [9, 10], it has been found that rats and seals use their mystacial vibrissae actively for tactile sensing. The FSC of some groups of vibrissae are motile due to specialized surrounding musculature [5, 6]. Using two types of muscles (intrinsic and extrinsic), an animal can repetitively move vibrissae back and forth (Fig. 2.2). This behaviour is known as whisking.

The vibrissal hair has no receptors along its length, since it made of dead material. Hence, all tactile signals at the tip of the vibrissa must be transmitted mechanically to sensory receptors inside the FSC. How vibrissae sense this information, and how it is encoded by the brain, are not known exactly, although the vibrissa system has been studied for over a century.

Nowadays, there are several competing hypotheses to understand the

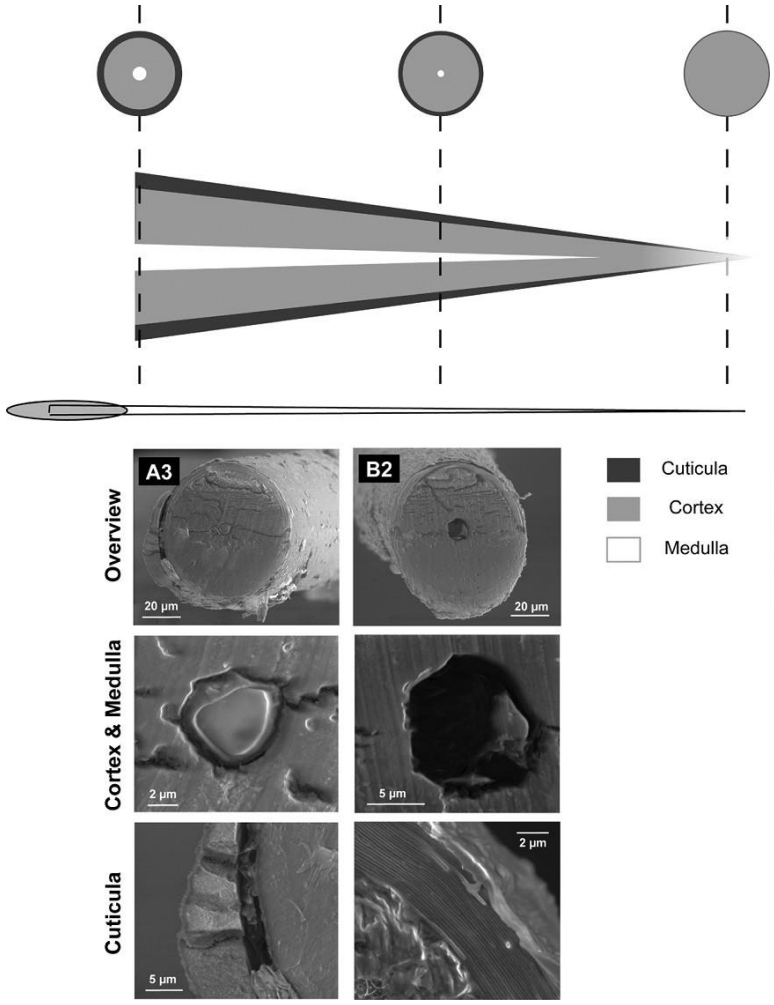

Figure 2.3: Top: share of components of a macro vibrissa at base, mid and tip. Bottom: pictures of cross-sections of two macro vibrissae [4]

mechanism of texture discrimination and tactile encoding by vibrissae. These hypotheses assume that mechanical interactions between the vibrissa and an object, as well as the shape of both, generate different complex patterns of vibrissa vibration and different coding strategies in the nervous system.

In the resonance hypothesis introduced in [3, 11, 12], vibrissae are regarded as elastic beams whose natural resonance frequency varies with parameters describing their structure (in particular, with length, radius, Young's modulus, etc.). When a vibrissa sweeps across a surface at a given velocity, the spatial texture generates vibrations of the vibrissa at a temporal frequency. Resonance vibrations are proposed to build up in vibrissae whose resonance frequency matches this temporal frequency of the surface structure. Because resonance frequency varies for vibrissae within one mystacial pad, each vibrissa is tuned to resonate for a specific range of textures. The amplification of tactile signals by resonance drives spatial neural activity in the sensors inside the FSC relative to the amplitude of resonance vibrations.

In the other hypotheses such as the mean speed theory [13, 14, 15] and the slip-stick theory [13, 16, 17], mechanical resonance properties of vibrissae play no special role in coding. Instead, the friction interaction between the vibrissal tip and surfaces generates complex, temporal patterns of vibrissa motion. These patterns represent mean speed of vibrissa vibration [15] and irregular high-velocity motions called vibrissa slips and sticks [13]. The texture coding in the sensory system follows these features of the patterns correlative by changing the fire rate of neural activity.

Which coding mechanism is exactly responsible for the tactile discrimination of different textures remains an open question [18]. Attempts to distinguish these hypotheses are made in [15, 16] by measuring vibrissae vibrations and neural responses in awake, behaving animals.

2.3 State of the art in modelling of vibrissae

From the engineering point of the view, the vibrissa as a biological object leads to the abstraction of rigid body models or elastic continuum models.

In [19], the movement of a rigid rod vibrissa in a pinned connection influenced by spring and damping elements is investigated theoretically. The authors in [1, 20, 21] improved rigid rod models for vibrissa due to the implementation of more complex boundary conditions. They introduce specific spring and damping elements considering the characteristics of the skin and the FSC (Fig. 2.4).

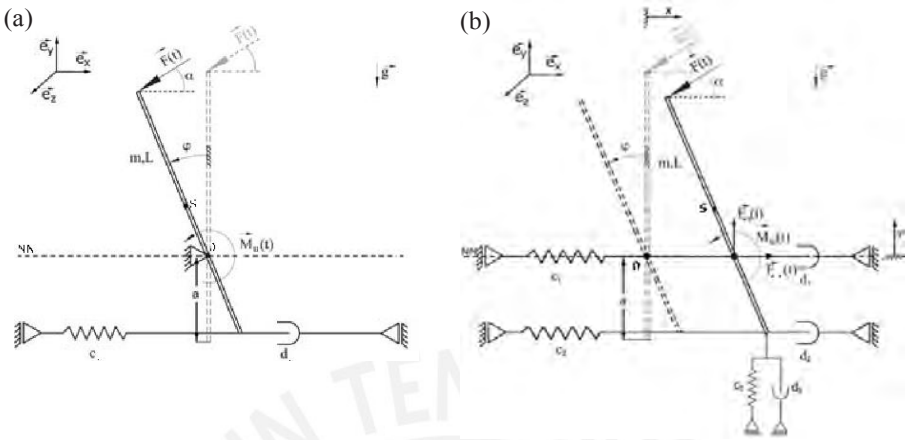

Figure 2.4: Mechanical models of the vibrissa as a rigid rod from [1, 20, 21]: a) model with one degree of freedom; b) model with three degrees of freedom.

Continuum models of a vibrissa as an elastic deformable beam following Hooke's law are closer to the biological paradigm, since they are able to take the inherent dynamical behaviour and the bending stiffness of the vibrissa into account, e.g.,[1, 8, 22] (Fig. 2.5).

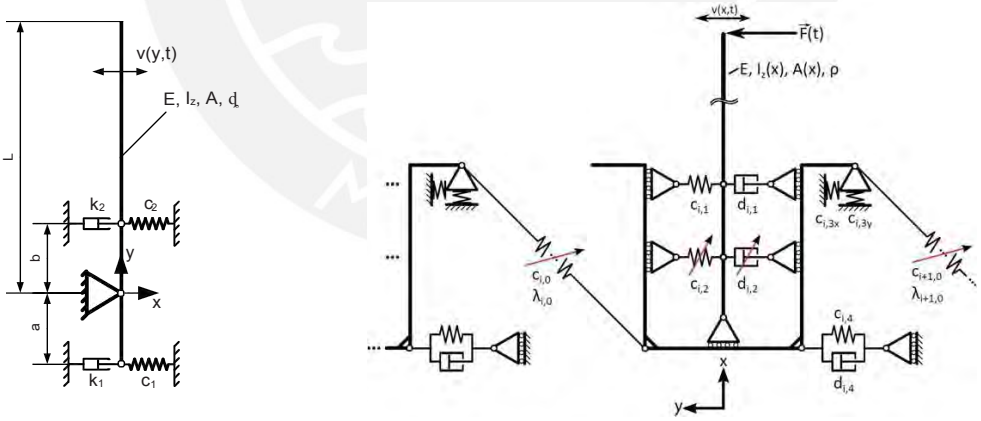

Figure 2.5: Mechanical models of the vibrissa with a high level of detail with regard to support conditions [1, 23]

Analytical investigations made in [24, 25] show that it is possible to reconstruct a profile contour by one single quasi-static sweep of the straight elastic beam along the object through the calculating the clamping forces and bending moment (Fig. 2.6).

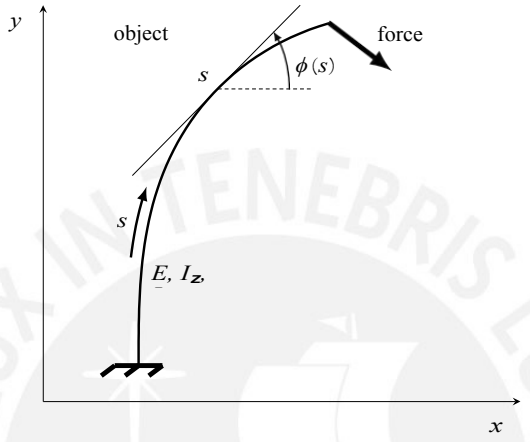

Figure 2.6: Elastic beam under large deflection for quasi-static object scanning [25]

Applications of tactile sensors following the functional principle of vibrissae is the recent focus in robotics. Figure 2.7 shows developed prototypes of mobile robot that use artificial tactile hairs for object localization.

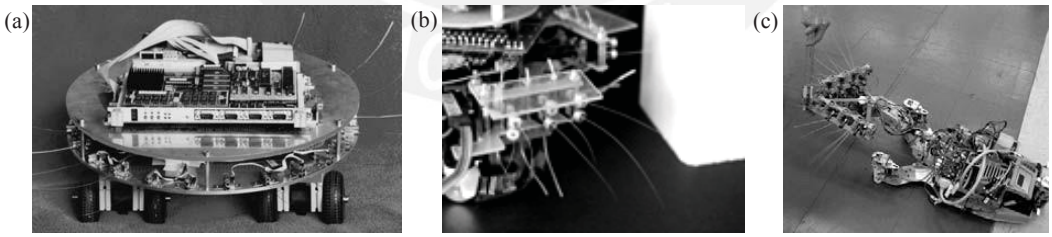

Figure 2.7: Examples of artificial tactile sensors in mobile robots: a) experimental platform [26]; b) mobile robot Amouse [28, 27]; c) SCHRATCHbot [29, 30]

2.4 Discussion

In the present thesis, I would like to concentrate on the resonance phenomenon of vibrissae vibrations during texture discrimination and the mechanical explanation of it.

As the vibrissa sweeps across an object, frictional interactions between the tip and a roughness profile generate oscillations of the vibrissal hair (Fig. 2.8). The arising friction force, like any other function of time, can be decomposed into the frequency components with the Fourier transform spectrum. The first several harmonic terms of it may sufficiently reproduce this force function. Further on, to investigate the phenomenon of parametric resonance, periodic force functions are of primal interest. In the theoretical and numerical investigations, the vibrissal hair will be modelled as an elastic Euler-Bernoulli beam. The following mechanical models will be considered: an elastic beam with the straight neutral axis and circular cross-section, and a curved elastic beam with the circular natural configuration and circular cross-section.

Throughout this work, it is assumed that the roughness profile exerts a cosinusoidal force $F(t) = F_0 \cos(\Omega t)$ that is applied perpendicular to the cross-section at the tip of the beam. The frequency Ω of the force coincides with one of the harmonic components. Results of the behavioural experiments with rats discriminating regular grooved plates are presented in [31].

Figure 2.9 shows the context of the thesis in the vibrissa research field.

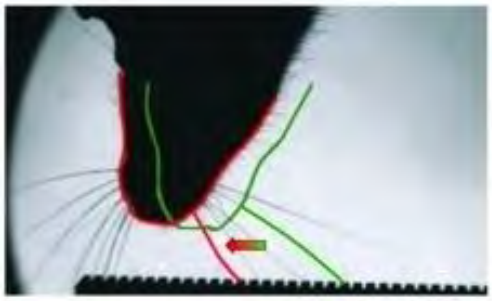

Figure 2.8: Vibrissae sweeping along the textured plate [31]

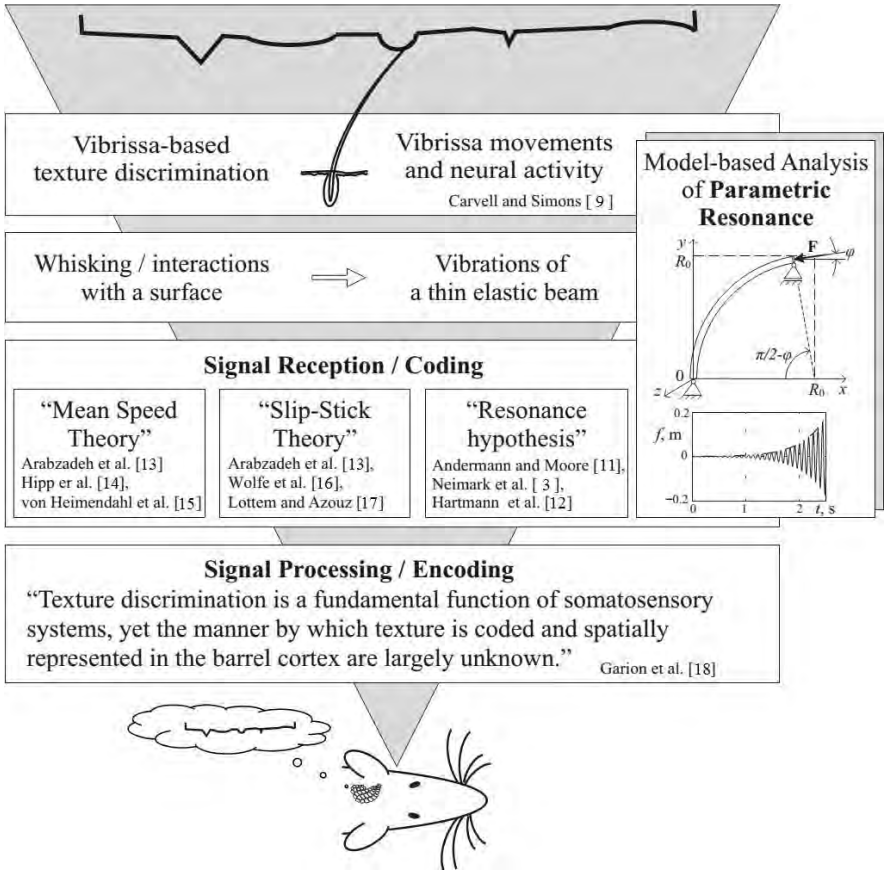

Figure 2.9: The context of the thesis in the vibrissa research field [32]

3 Resonance phenomenon

In physics, resonance is the tendency of a system to respond at greater amplitude at a specific preferential frequency. It is caused by the possibility of a system to store and transfer energy between two or more different storage modes. Resonance phenomena develop with all types of vibrations or waves. There is mechanical resonance, acoustic resonance, electromagnetic resonance, etc. Resonant systems can be used to originate vibrations of a specific frequency, or analyze specific frequencies from a complex vibration containing many frequencies. However, resonance may cause volient catastrophic failure of systems (bridges, buildings and airplanes, etc.). This phenomenon is known as resonance disaster (Fig. 3.1).

Figure 3.1: Collapse of the Tacoma Narrows Bridge in Washington [33]

3.1 Resonance in forced vibrations

Consider one type of vibrations, where an external time-varying force $\dot{F}(t)$ is applied to a system. The simplest form of the force $\dot{F}(t)$ is harmonical. In all real systems, energy is dissipated, which means the system is damped. But often the damping is very small, so we consider systems without damping. Such forced undamped systems with one degree of freedom (DOF) are shown in Fig. 3.2.

The derivation of the equation of motion is achieved by considering forces acting on a mass point, when it is regarded as a free body. Forced vibrations

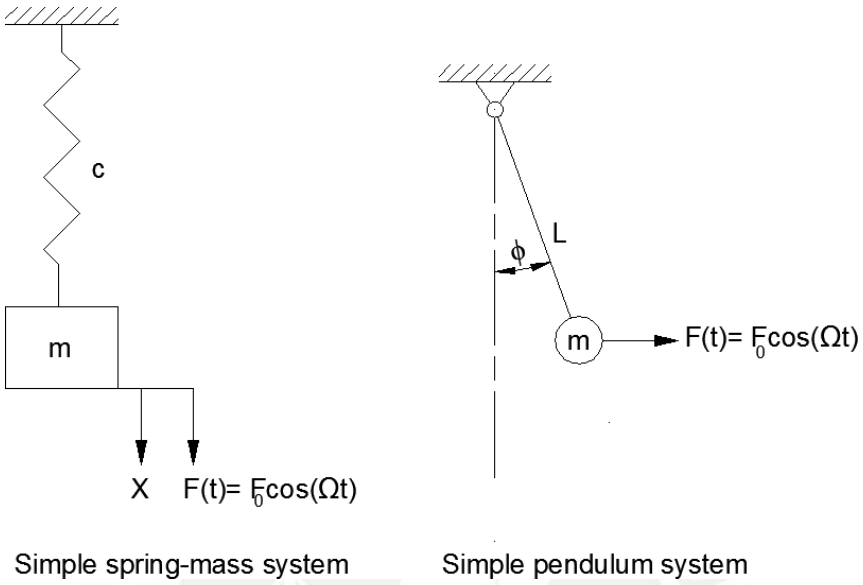

Figure 3.2: Forced undamped systems with 1 DOF

of a simple spring-mass system with 1 DOF are described by the following equation:

$$\ddot{x}(t) + \omega_0{}^2 x(t) = \frac{F_0}{m} \cos(\Omega t), \tag{3.1}$$

where $\omega_0 = \sqrt{c/m}$ is called the undamped natural frequency of free vibrations, m is the mass of the system, c is the stiffness of the spring, F_0 is the amplitude of the force, and Ω is the excitation frequency.

Equation (3.1) is an inhomogeneous linear second-order differential equation with constant coefficients. The solution of it is the sum of two parts: the homogeneous solution $x_h(t)$ and the particular solution $x_p(t)$. The homogeneous solution is obtained by setting the right-hand side of the equation (3.1) equal to 0:

$$\ddot{x}_h(t) + \omega_0{}^2 x_h(t) = 0. \tag{3.2}$$

A solution of (3.2) describes harmonic, undamped, free vibrations of the mass, and it has the following form:

$$x_h(t) = A \cos(\omega_0 t - \varphi), \tag{3.3}$$

where the constant A is the amplitude of response and φ is the phase angle.

A particular solution of the equation (3.1) is obtained by assuming

$$x_p(t) = B\cos(\Omega t), \tag{3.4}$$

where B is an unknown constant. Substituting it into equation (3.1), we find

$$B = \frac{F_0/m}{\omega_0^2 - \Omega^2}, \tag{3.5}$$

and the required particular solution becomes

$$x_p(t) = \frac{F_0/m}{\omega_0^2 - \Omega^2}\cos(\Omega t). \tag{3.6}$$

Thus, the complete solution of the equation (3.1) is the sum of (3.3) and (3.6):

$$x(t) = A\cos(\omega_0 t - \varphi) + \frac{F_0/m}{\omega_0^2 - \Omega^2}\cos(\Omega t). \tag{3.7}$$

The arbitrary constants A and φ are found from the initial conditions $x(0) = x_0$ and $\dot{x}(0) = \dot{x}_0$.

It is seen that a system under the action of the periodic force executes a motion, which is a combination of two oscillations. The first term of (3.7) represents free vibrations with the natural frequency ω_0. The second term corresponds to the forced vibrations of the system with the external frequency Ω. The structure of the particular solution $x_p(t)$ depends on the relation between ω_0 and Ω. Defining $\gamma = \Omega/\omega_0$, equation (3.6) takes the form

$$x_p(t) = \frac{F_0}{c(1 - \gamma^2)}\cos(\Omega t). \tag{3.8}$$

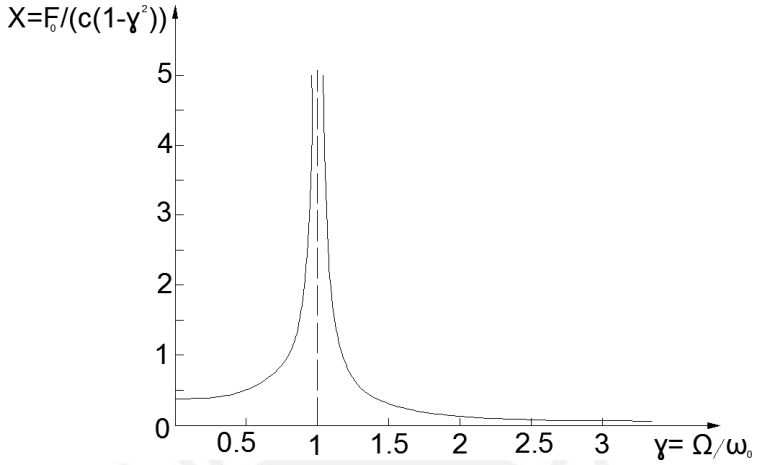

Figure 3.3: Frequency response of an undamped system

In this expression, (F_0/c) represents the displacement that the disturbing force would produce, if acting statically, and the factor $cos(\Omega t)/(1-\gamma^2)$ accounts for the dynamic nature of the force $\dot{F}(t)$. Fig. 3.3 shows the dependence of the amplification ratio $X = F_0/(c(1-\gamma^2))$ on the frequency ratio $\gamma = \Omega/\omega_0$.

When the external forcing frequency Ω nears the natural frequency of the system ω_0 ($\gamma \approx 1$), the amplitude of forced vibrations rapidly increases and gets extremely high. This phenomenon is called ***resonance***.

Consider the case of resonance, when a system is excited with the resonant frequency $\Omega = \omega_0$. Then, the particular solution of the inhomogeneous equation (3.1) has the form:

$$x_p(t) = \frac{F_0}{2m\omega_0} t \sin(\omega_0 t). \qquad (3.9)$$

It means that the amplitude of oscillations in resonance grows proportional with the time. It should be noticed that the resonance takes place even when initial conditions are exactly zero ($x(0) = 0$ and $\dot{x}(0) = 0$). The graph of the resonance response of a system is shown in Fig. 3.4.

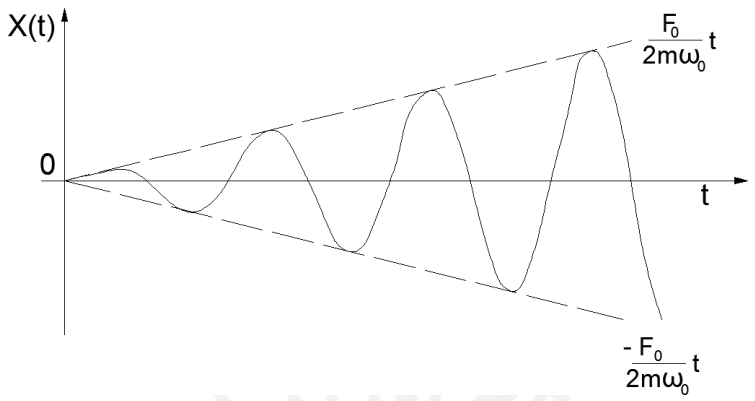

Figure 3.4: Response of the system in the case of resonance ($\Omega = \omega_0$) for $x(0) = 0,\ \dot{x}(0) = 0$

3.2 Parametric resonance

Forced vibration problems do not show parameter variation as a result of imposed forcing. Another possibility to excite nondamping vibrations is to periodically change some system parameters to which the system is sensitive. For certain relationships between the disturbing frequency Ω and the natural frequency of a system ω_0, the amplitude of these vibrations increases rapidly to large values. This phenomenon is called ***parametric resonance***. Physical systems exhibiting potential parametric vibrations effects are shown in Fig. 3.5.

Motion of such systems with 1 DOF is generally described by an ordinary linear second-order differential equation of the form:

$$\ddot{x}(t) + \omega^2(t)x(t) = 0, \tag{3.10}$$

where the coefficient $\omega^2(t)$ of x is not constant: it depends explicitly on time t. In the case of periodic changes of the parameter ω, when $\omega(t + T) = \omega(t)$, the corresponding differential equation (3.10) is called Hill equation, who introduced it in 1886 [36].

For example, for a simple pendulum, whose support O is vertically excited as $y(t) = y_0 \cos(\Omega t)$ (Fig. 3.5, right), its motion is described by

$$\frac{d}{dt}(ml^2\dot{\theta}(t)) = -m(\ddot{y}(t) + g)l\sin(\theta(t)).$$

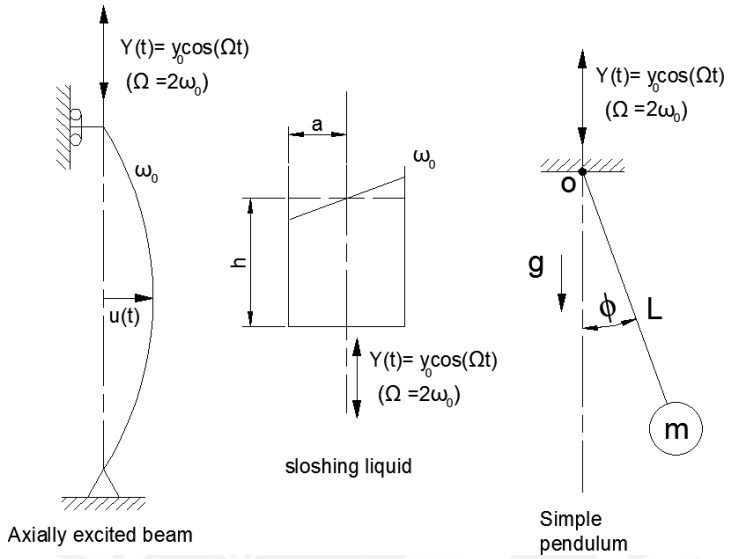

Figure 3.5: Examples of physical systems exhibiting parametrical resonance [34]

Here, m is the mass of the pendulum, l is the length, g is the gravitational acceleration and $\theta(t)$ is the angular displacement.

For small angle approximation, we have

$$\ddot{\theta}(t) + \left(\frac{g}{l} - \frac{y_0\Omega^2}{l}\cos(\Omega t)\right)\theta(t) = 0. \qquad (3.11)$$

The natural frequency of the pendulum is $\omega_0 = \sqrt{g/l}$. Defining the dimensionless time $\tau = t\omega_0$, the equation (3.11) can be written as

$$\ddot{\theta}(\tau) + (1 - \varepsilon\cos(\gamma\tau))\theta(\tau) = 0 \qquad (3.12)$$

with the dimensionless parameters $\varepsilon = y_0\Omega^2/g$ and $\gamma = \Omega/\omega_0$. Equation (3.12) is the special case of Hill equation (3.10) with the cosinusoidal time dependency of the parameter. It is called Mathieu equation. A complete mathematical analysis of its solution is out of the scope of the present thesis. The theory of Mathieu equation has been fully developed and all significant properties of its solutions are well known [37, 38].

It appears that there are transition values depending on the parameters ε and γ, which identify the boundaries of parameter values resulting in

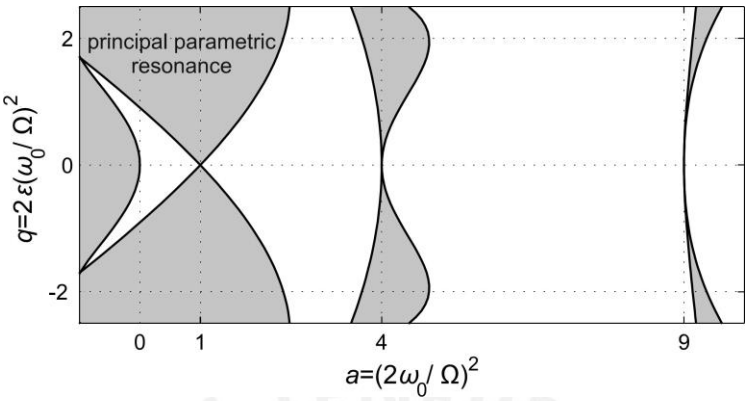

Figure 3.6: Ince-Strutt diagram of the Mathieu equation (3.12) indicating the transition curves, which divide the a-q plane in stable (white) and unstable (grey) regions

stable or unstable behaviour. For the unstable case, arbitrarily small deviations of a system produce a large response and the amplitude increases progressively in time. The transition curves dividing the plane of parameters $a = (2\omega_0/\Omega)^2$ and $q = 2\varepsilon(\omega_0/\Omega)^2$ in stable and unstable regions are shown by the Ince-Strutt diagram in Fig. 3.6.

It can be seen that there are many intervals of the frequency where the parametric resonance takes place. But the most intensive resonance response of the system occurs, when the forcing frequency is twice the natural frequency: $\Omega \approx 2\omega_0$. This range is called the region of ***principal parametric resonance***, and the width of this region is proportional to the parameter ε:

$$2 - \frac{\varepsilon}{2} < \frac{\Omega}{\omega_0} < 2 + \frac{\varepsilon}{2}. \tag{3.13}$$

The other frequency ranges of the parametric resonance are close to the values of the form $\Omega = 2\omega_0/n$ for any natural number n. However, the width of these regions gets narrow proportionally to the value ε^n as n increases.

In contrast to the resonance in forced vibrations, parametric resonance can only occur if at least small vibrations already exist in the system. It may cause the instability of the bottom equilibrium position of the pendulum with the exponentially increasing amplitude to infinity (Fig. 3.7).

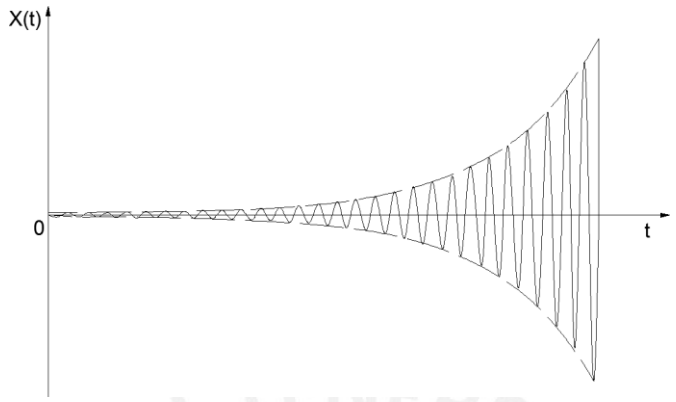

Figure 3.7: Response of the system in the case of the parametric resonance for $x(0) \neq 0$

4 Theoretical analysis of parametric vibrations of a truncated conical beam

In this thesis, the following abbreviations are used to indicate different beam models:

- Model 1 — a straight cylindrical beam (SCB),
- Model 2 — a truncated conical beam (TCB),
- Model 3 — a circular cylindrical beam (CCB).

4.1 Formulation of the problem

A beam is a slender structural element spanning a distance between one or more supports and subjected to external loads that cause primarily bending. The beam is characterized by its profile (shape of cross-section), length, and material properties. Fig. 4.1 shows a simply supported beam of a length L with a circular cross-section. The Cartesian coordinate system $(0, x, y, z)$ is placed such that the x axis coincides with the underformed straight axis of symmetry of the beam. The material properties of the beam are constant. The radius of the circular cross-section develops linearly along the axial direction: $r(x) = r_b + (r_t - r_b)x/L$, where r_b and r_t are the radii at the base and the tip of the beam respectively. The mass of a beam's element is $m_0(x) = \rho\pi r^2(x)$, where ρ = const is the density and E = const is the Young's modulus. The moment of inertia of the cross-section is defined as $I_z(x) = \pi r(x)^4/4$.

This geometry corresponds to the Model 2 of a TCB. In the case $r_b = r_t$, it satisfies the Model 1 of SCB.

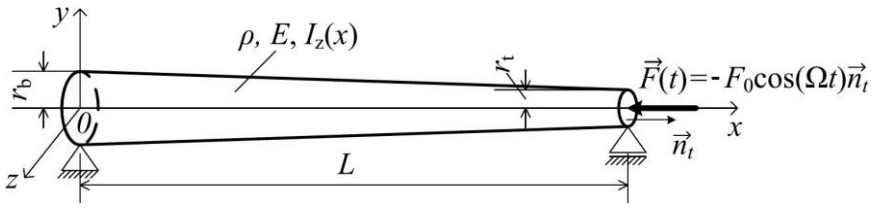

Figure 4.1: Model of the TCB under an applied periodic force

The beam is simple supported at the base $x = 0$ and at the tip $x = L$. A time-varying periodic force $\dot{F}(t) = -F_0 \cos(\Omega t)\dot{n}_t$ is applied perpendicularly to the cross-section at the tip of the beam causing it to oscillate at a specific frequency. Here, $\dot{n}_t$ is the normal to the cross-section at $x = L$.

4.2 Euler-Bernoulli beam theory

There are distinct relationships between the load on a beam, the resulting internal forces, moments and the corresponding deformation. A theory often used is the Euler-Bernoulli beam theory. It assumes that the strain tensor is a linear function of displacement gradient components, see [39, 40]. Experiments have shown that strains developed along the depth of a cross-section of the beam vary linearly. The strain at the top or bottom of the cross-section is maximal and decreases with the depth, becoming zero at a certain distance from the surface. The axis, where the stress is zero, is called the neutral axis. If the cross-section is symmetric, isotropic and is not curved before a load occurs, then the neutral axis is at the geometric centroid.

The Euler-Bernoulli beam theory takes the bending moment into account and neglects the effect of transverse shear deflections and rotary inertia. Thus, the major assumptions are:

- The cross-section rotates around a neutral axis remaining plane.
- The cross-section remains perpendicular to the neutral axis during deformation.

Consider a differential element of the beam with a length dx isolated by two adjoining cross-sections (Fig. 4.2). The forces acting on the element are the normal force $\dot{N}(x, t)$, the transverse shear force $\dot{Q}_y(x, t)$, and the bending moment $\dot{M}_{bz}(x, t)$. From the elementary theory of beam, the relationship between bending moment and deflection can be expressed as [41]

$$M_{bz}(x, t) = EI_z(x) \frac{\partial^2 v(x, t)}{\partial x^2}. \tag{4.1}$$

The transverse shear force $\dot{Q}_y(x, t) = Q_y(x, t)\dot{e}_y$ is

$$Q_y(x, t) = -\frac{\partial M_{bz}(x, t)}{\partial x}. \tag{4.2}$$

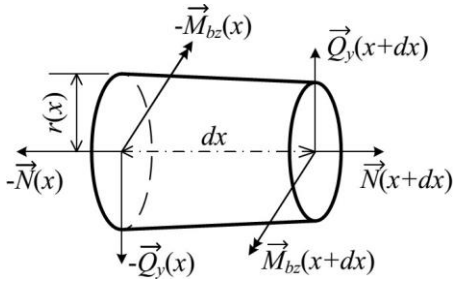

Figure 4.2: Free-body diagram of a beam element of infinitesimal length dx with external actions upon it

Here, $\dot{e}_x$, $\dot{e}_y$, $\dot{e}_z$ are Cartesian basic vectors, and $v(x, t)$ is the transverse displacement.

The equation governing small transverse vibrations of a straight Euler-Bernoulli beam in the x-y plane subjected to an external load $q(x, t)$, without damping is [39]:

$$m_0(x)\frac{\partial^2 v(x,\,t)}{\partial t^2} + \frac{\partial^2}{\partial x^2}\left[EI_z(x)\frac{\partial^2 v(x,\,t)}{\partial x^2}\right] = q(x,\,t). \tag{4.3}$$

This is the partial differential equation for the transverse displacement $v(x, t)$ of the beam in y direction. The bending moment and shear force in the beam can be calculated from (4.1) and (4.2) after the deflection due to a given load has been determined.

4.3 Natural frequencies and modes of an Euler-Bernoulli beam

In the absence of the load $q(x, t)$, we have free vibrations of the beam. In this case, the equation of motion (4.3) is

$$m_0(x)\frac{\partial^2 v(x,\,t)}{\partial t^2} + \frac{\partial^2}{\partial x^2}\left[EI_z(x)\frac{\partial^2 v(x,\,t)}{\partial x^2}\right] = 0. \tag{4.4}$$

We attempt a solution using decomposition of the displacement of the form

$$v(x,\,t) = X(x)T(t). \tag{4.5}$$

Then, the partial derivatives are

$$\frac{\partial^2 v(x,t)}{\partial t^2} = X(x)\ddot{T}(t), \qquad \frac{\partial^2 v(x,t)}{\partial x^2} = X''(x)T(t), \tag{4.6}$$

where the "." notation is the derivative with respect to time, and the " ′ " notation is the derivative with respect to the x coordinate.

The equation (4.4) of free vibrations can be written as:

$$m_0(x)X(x)\ddot{T}(t) + T(t)\,[EI_z(x)X''(x)]'' = 0, \tag{4.7}$$

which, when divided by $m_0(x)X(x)T(t)$, becomes

$$-\frac{\ddot{T}(t)}{T(t)} = \frac{[EI_z(x)X''(x)]''}{m_0(x)X(x)}. \tag{4.8}$$

For equation (4.8) to be valid for all values of x and t, the two expressions must therefore be constant, say ω^2 = const. Thus, the partial differential equation (4.4) splits into two ordinary differential equations: one governing the time function $T(t)$ and the other governing the spatial function $X(x)$.

$$\ddot{T}(t) + \omega^2 T(t) = 0, \tag{4.9}$$

$$[EI_z(x)X''(x)]'' - \omega^2 m_0(x)X(x) = 0. \tag{4.10}$$

Equation (4.9) has the same form as the equation governing free vibration of a system with 1 DOF with natural frequency ω (compare with (3.2)). The general solution for the time-dependent function can be written as:

$$T(t) = D_1 \sin(\omega t) + D_2 \cos(\omega t), \tag{4.11}$$

where D_1 and D_2 are unknown constants. For any given stiffness and mass functions, $EI_z(x)$ and $m_0(x)$, respectively, there is an infinite set of frequencies ω and associated modes $X(x)$ that satisfy the eigenvalue problem defined by equation (4.10) and the corresponding boundary conditions of the beam.

Model 1 — Straight cylindrical beam (SCB)

For the special case of the SCB (Model 1), when $EI_z(x) = EI_z$ = const and $m_0(x) = m_0$ = const, the equation (4.10) can be written as:

$$EI_z X''''(x) - \omega^2 m_0 X(x) = 0. \tag{4.12}$$

The general solution of the above equation is

$$X(x) = C_1 \sin(\beta x) + C_2 \cos(\beta x) + C_3 \sinh(\beta x) + C_4 \cosh(\beta x), \qquad (4.13)$$

where

$$\beta^4 = \frac{\omega^2 m_0}{EI_z}. \qquad (4.14)$$

This solution contains four unknown constants, C_1, C_2, C_3, and C_4. They are unique for a given set of boundary condition and the eigenvalue parameter β.

Uniform simply supported beam

For an uniform simple supported beam (Fig. 4.1), the displacements and the bending moments at $x = 0$ and $x = L$ are zero (see (4.15)):

$$v(0, t) = 0, \quad \frac{\partial^2 v(0, t)}{\partial x^2} = 0, \quad v(L, t) = 0, \quad \frac{\partial^2 v(L, t)}{\partial x^2} = 0. \qquad (4.15)$$

Then, using the first two boundary conditions, gives $C_2 = C_4 = 0$, and the general solution reduces to

$$X(x) = C_1 \sin(\beta x) + C_3 \sinh(\beta x). \qquad (4.16)$$

Substituting it to the last two conditions of (4.15), it follows

$$C_3 \sinh(\beta L) = 0. \qquad (4.17)$$

The multiplier $\sinh(\beta L)$ cannot be zero. Otherwise, ω would be zero too, i.e., a trivial solution implying no vibration at all. So, the coefficient C_3 must be zero. This leads to the frequency equation:

$$C_1 \sin(\beta L) = 0. \qquad (4.18)$$

The equation can be satisfied by selecting $C_1 = 0$, which gives $X(x) = 0$, i.e. a trivial solution. Therefore, $\sin(\beta L) = 0$, from which

$$\beta L = n\pi, \quad n = 1, 2, 3, \ldots \qquad (4.19)$$

Equations (4.14) and (4.19) then give the corresponding natural vibration frequencies:

$$\omega_n = \frac{n^2\pi^2}{L^2} \sqrt{\frac{EI_z}{m_0}}, \quad n = 1, 2, 3, \ldots \qquad (4.20)$$

The natural vibration mode $X_n(x)$ corresponding to each ω_n is obtained by substituting equation (4.19) in (4.16) with $C_3 = 0$ as determined earlier:

$$X_n(x) = C_1 \sin\left(\frac{n\pi x}{L}\right). \tag{4.21}$$

The value of C_1 may be arbitrary. For example, $C_1 = 1$ makes the maximum value of $X_n(x)$ equal to unity. The first four natural modes of the SCB are shown in Fig. 4.3.

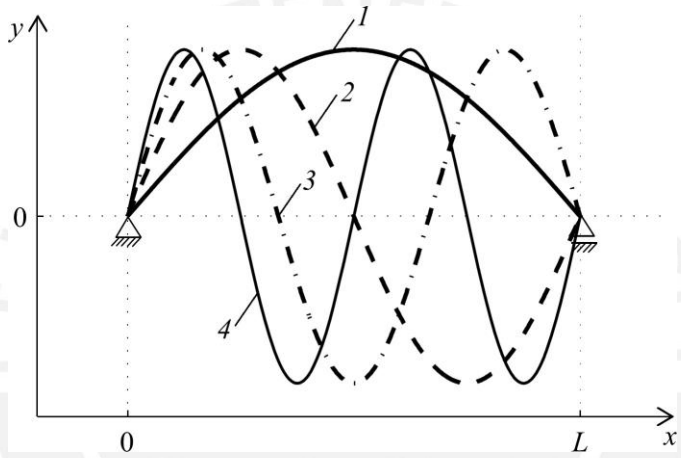

Figure 4.3: Four mode shapes of the simply supported SCB (Model 1)

Model 2 — Truncated conical beam (TCB)

To find natural vibration frequency of the TCB, the Rayleigh's method, based on Rayleigh's quotient, can be applied [42].

$$R(\omega_0) = \omega_0^2 \approx \frac{\int_0^L EI_z(x)\left(\frac{d^2v(x)}{dx^2}\right)^2 dx}{\int_0^L \rho A(x) v^2(x) dx}. \tag{4.22}$$

The deflection shape of the beam, which satisfies the boundary conditions (4.15), is

$$v(x) \approx \tilde{v}(x) = x(x^3 - 2Lx^2 + L^3). \tag{4.23}$$

Substituting the corresponding values, then for the spacial case of the TCB, when $r_t = r_b/2$, the Rayleigh's quotient gives the formula for the first natural vibration frequency:

$$\omega_0 \approx 3.849 \frac{r_b}{L^2} \sqrt{\frac{\overline{E}}{\rho}}. \tag{4.24}$$

This formula gives an upper boundary value for the first eigenfrequency.

4.4 Timoshenko beam theory

The Timoshenko theory takes into account the rotary inertia, shear deformation and their combined effects [43]. Cross-sections are still assumed to remain plane in this development. In contrast to the Euler-Bernoulli beam theory, the cross-section is no longer constrained to remain perpendicular to the neutral axis (Fig. 4.4).

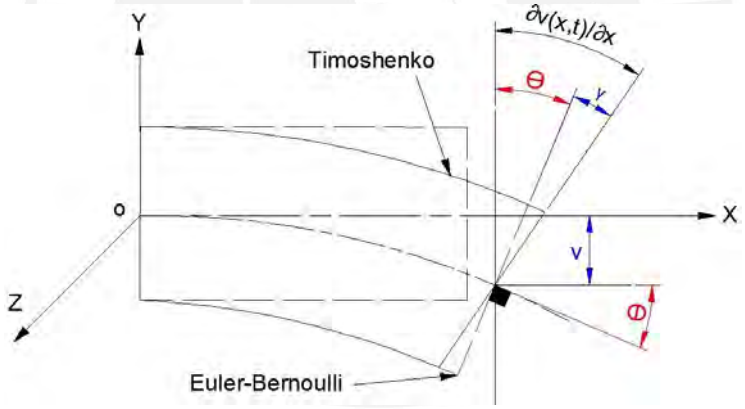

Figure 4.4: Euler-Bernoulli beam theory and Timoshenko beam theory

The exact solution of the beam vibration problem requires the deflection due to the shear stress to be considered. So, the angle $\partial v(x, t)/\partial x$ between the beam axis and the x axis is a sum of the angle $\theta(x, t)$ due to pure bending and the shear angle $\gamma(x, t)$, i.e.:

$$\frac{\partial v(x, t)}{\partial x} = \theta(x, t) + \gamma(x, t). \tag{4.25}$$

Another factor that affects the transverse vibration of the beam, is the fact that each section of the beam rotates slightly in addition to its lateral motion, when the beam deflects. The influence of the beam section rotation is taken into account through the rotary inertia of the beam's element:

$$\rho I_z(x)\frac{\partial^2\theta(x,\,t)}{\partial t^2}dx.$$

The bending moment $\dot{M}_{bz}(x,\,t) = M_{bz}(x,\,t)\dot{e}_z$ and the transverse shear force $\dot{Q}_y(x,\,t) = Q_y(x,\,t)\dot{e}_y$ are related to θ and v by the expressions:

$$M_{bz}(x,t) = EI_z(x)\frac{\partial\theta(x,\,t)}{\partial x}, \tag{4.26}$$

$$Q^y(x,\,t) = kGA(x)\left[\theta(x,\,t) - \frac{\partial v(x,\,t)}{\partial x}\right]. \tag{4.27}$$

Here, G is the shear modulus, A is the cross-section area, EI_z is the bending stiffness, k is Timoshenko shear coefficient depending on the shape of the cross-section. It is within the range [0.5, 1]. For the circular cross-section of the beam k=0.9 [44]

By applying d'Alembert's principle, the system of coupled differential equations for transverse vibration of the Timoshenko beam subjected to an external load $q(x,\,t)$ is given by

$$\begin{aligned} m_0\frac{\partial^2 v}{\partial t^2} + \frac{\partial}{\partial x}\left[kGA\left(\theta - \frac{\partial v}{\partial x}\right)\right] &= q(x,\,t), \\ \rho I_z\frac{\partial^2\theta}{\partial t^2} = \frac{\partial}{\partial x}\left[EI_z\frac{\partial\theta}{\partial x}\right] - kGA\left(\theta - \frac{\partial v}{\partial x}\right), \end{aligned} \tag{4.28}$$

where $m_0(x)$ is the mass of the beam, $v(x,t)$ is the transverse displacement.

By solving the first equation (4.28) for $\partial\theta/\partial x$ and substituting the result into the second one, we obtain the equation of motion of an uniform, isotropic beam of constant cross-section ($m_0(x) = \rho A$ = const, EI_z = const):

$$\begin{aligned} EI_z\frac{\partial^4 v}{\partial x^4} + \rho A\frac{\partial^2 v}{\partial t^2} - \rho I_z\left[1 + \frac{E}{kG}\right]\frac{\partial^4 v}{\partial x^2\partial t^2} + \frac{\rho^2 I_z}{kG}\frac{\partial^4 v}{\partial t^4} = \\ \frac{\rho I_z}{kGA}\frac{\partial^2 q(x,\,t)}{\partial t^2} - \frac{EI_z}{kGA}\frac{\partial^2 q(x,\,t)}{\partial x^2} + q(x,\,t). \end{aligned} \tag{4.29}$$

4.5 Natural frequencies of Timoshenko beam

For the case of free vibration $q(x, t) = 0$, equation (4.29) becomes

$$EI_z \frac{\partial^4 v}{\partial x^4} + \rho A \frac{\partial^2 v}{\partial t^2} - \rho I_z \left(1 + \frac{E}{kG}\right) \frac{\partial^4 v}{\partial x^2 \partial t^2} + \frac{\rho^2 I_z}{kG} \frac{\partial^4 v}{\partial t^4} = 0. \qquad (4.30)$$

Consider a solution of the form

$$v(x, t) = C \sin\left(n\pi \frac{x}{L}\right) \sin(\omega_n^j t), \qquad (4.31)$$

which satisfies the necessary boundary conditions at $x = 0$ and $x = L$, when both ends are simply supported. Here, C is a constant, ω_n^j is the nth natural frequency of a Timoshenko beam.

Denoting a natural frequency of the Euler-Bernoulli beam, when both the effects of rotary inertia and shear deformation are neglected, by ω_n (see equation (4.20)), and defining $\Omega_n = \omega_n^j/\omega_n$, the frequency equation can be written as:

$$\left(1 - \Omega_n^2\right)\left(1 - \Omega_n^2 \left(\frac{n\pi r}{L}\right)^2 \left(1 + \frac{E}{kG}\right)\right) + \Omega_n^4 \left(\frac{n\pi r}{L}\right)^4 \frac{E}{kG} = 0, \qquad (4.32)$$

where $r^2 = I_z/A$.

It can be seen that the equation (4.32) is a quadratic equation in Ω_n^2, and for any given n there are two values of Ω_n that satisfy this equation. The smaller value corresponds to the bending deformation mode, while the larger one corresponds to the shear deformation mode [44]. Figure 4.5 shows the dependence of the ratio Ω_n on nr/L for three values of E/kG.

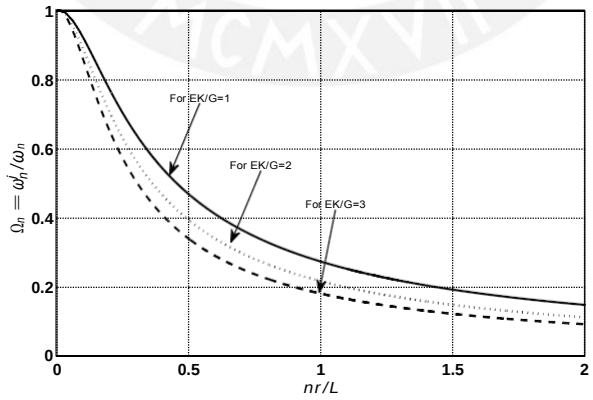

Figure 4.5: Variation of frequency

It may be seen that when nr/L 1, equation (4.32) reduces to $\Omega_n \approx 1$, i.e. $\omega_n^{\text{j}} \approx \omega_n$.

4.6 Governing equation of the beam and its approximation

Consider small transverse vibrations of the beam about its straight equilibrium configuration in the x-y plane and in the absence of a force of viscous damping. That means that the displacement $v(x, t)$ in the y direction and its derivative are of the first order of smallest (Fig. 4.6). The inertia forces associated with the rotation of the cross-section of the beam with respect to its own principal axis and the shear deformation are not taken into account. So, the Euler-Bernoulli beam theory is considered. Since the longitudinal inertia forces can substantially influence the dynamic stability of the beam only in the case, where the frequency of the external force is near the longitudinal natural frequencies of the beam, we consider that the system is not close to the resonance of the longitudinal vibrations [45].

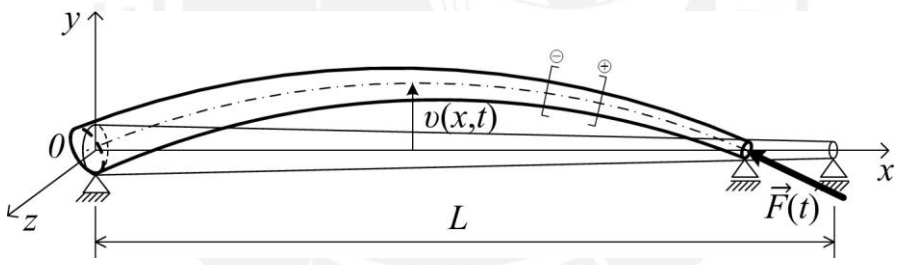

Figure 4.6: Deflection of the TCB under the periodic force acting on the tip

The transverse motion of the beam under an applied periodic force $\dot{F}(t) = \_F_0 \cos(\Omega t)\dot{n}_t$, which is applied perpendicularly to the cross-section at the tip of the beam, is described by the following equation [46]:

$$Ł(v) = 0, \tag{4.33}$$

where

$$Ł(v) = m_0(x)\frac{\partial^2 v(x,\ t)}{\partial t^2} + \frac{\partial^2}{\partial x^2}\left[EI_z(x)\frac{\partial^2 v(x,t)}{\partial x^2}\right] + F_0\cos(\Omega t)\frac{\partial^2 v(x,\ t)}{\partial x^2}.$$

The beam can not experience any displacements and bending moment at the base $x = 0$, and the support conditions at the tip of the beam $x = L$ allow small displacements only in the horizontal direction. Since no external bending moment is applied at the tip, the bending moment at that location is zero. Consequently, we have the following boundary conditions for the function $v(x, t)$ itself as well as for the second derivative of it (see (4.1)):

$$v(0, t) = 0, \quad \frac{\partial^2 v(0, t)}{\partial x^2} = 0, \quad v(L, t) = 0, \quad \frac{\partial^2 v(L, t)}{\partial x^2} = 0. \tag{4.34}$$

To solve equation (4.33) Galerkin's Method is used, that is a method for finding the approximate solution of a differential equation [47]. This powerful method allows to reduce a partial differential equation to an ordinary one. The basic idea of the method of Galerkin is the following. It is required to determine the solution of the equation $L(v) = 0$, which satisfies boundary conditions (4.34). We shall seek an approximate solution of the equation in the form:

$$\tilde{v}(x, t) = \sum_{i=1}^{n} c_i \phi_i(x) f_i(t), \tag{4.35}$$

where $\phi_i(x), i = 1, ..., n,$ is a certain system of chosen basis functions satisfying the boundary conditions, and c_i are undetermined coefficients. Consider the functions $\phi_i(x)$ to be linearly independent. In order that $\tilde{v}(x, t)$ be the solution of the equation $L(v) = 0$, it is necessary that $L(\tilde{v})$ be identically equal to zero. This requirement is equivalent to the condition of the orthogonality of $L(\tilde{v})$ to all the functions of the system $\phi_i(x), i = 1, ..., n$. Stating these conditions, the linear system of n equations for the determination of the coefficients c_i follows

$$\int_0^L \left[L\left(\sum_{i=1}^{n} c_i \phi_i(x) f_i(t) \right) \right] \phi_i(x) dx = 0, \quad i = 1, ..., n. \tag{4.36}$$

Thus, substituting c_i in the expression for $\tilde{v}(x, t)$, the required approximate solution can be obtained. Here, a one-term approximation by Galerkin's Method of the equation (4.33) in the form $\tilde{v}(x, t) = \sin(\pi x/L) f(t)$ is assumed. It satisfies the pinned-pinned boundary condition of the beam (4.34).

Substituting this expression for $\tilde{v}(x, t)$ in equation (4.33), we obtain an ordinary second-order differential equation written in dimensionless form as

$$\ddot{f}(\tau) + [1 - \varepsilon \cos(\gamma \tau)] f(\tau) = 0, \tag{4.37}$$

where:

$$\varepsilon = \frac{2\pi L^2}{a_1 E r_b^4} F_0, \quad \gamma = \Omega \sqrt{\frac{4a_0 \rho L^4}{a_1 E r_b^2}}, \quad \tau = t \sqrt{\frac{a_1 E r_b^2}{4a_0 \rho L^4}}, \quad \delta = \frac{r_t}{r_b}, \quad 0 \le \delta \le 1,$$

$$a_0 = \frac{1}{6}(1 + \delta + \delta^2) - \frac{1}{4\pi^2}(1 - \delta)^2 > 0, \tag{4.38}$$

$$a_1 = \frac{\pi^4}{10}(1 + \delta + \delta^2 + \delta^3 + \delta^4) - \frac{\pi^2}{2}(1 - \delta)(1 - \delta^3) + \frac{3}{4}(1 - \delta)^4 > 0.$$

Equation (4.37) with periodic coefficient has the same form as the Mathieu equation (3.12), which describes parametrically excited vibrations. A periodic solution of (4.37) correspond to specific values of the dimensionless parameters ε and γ. Let us further determine the conditions of the parametric resonance, that is, the ranges of the parameters ε and γ, when the beam performs oscillations whose amplitude increases progressively .

4.7 The procedure of averaging and the principle range of the parametric resonance

According to [2], for an approximate analysis of a non-linear oscillating process described by (4.37), the method of averaging is used, when the exact differential equation of the motion is replaced by its averaged version [48]. To use this method, it is first needed to reduce (4.37) to the standard form by a change of variables. If we put $\varepsilon = 0$ in (4.37), then it describes a simple harmonic vibration with dimensionless natural frequency equal to unity. The general solution is $f(\tau) = a \cos(\tau + \theta)$, where constants a and θ, represent the amplitude and phase respectively, which are determined from the initial conditions. The solution to the perturbed equation (when $\varepsilon = 0$) is sought in the same form, but now a and θ are allowed to vary with τ:

$$f(\tau) = a(\tau) \cos(\tau + \theta(\tau)). \tag{4.39}$$

By following the method [48], an additional condition on the functions $a(\tau)$ and $\theta(\tau)$ is imposed:

$$\dot{f}(\tau) = -a(\tau) \sin(\tau + \theta(\tau)). \tag{4.40}$$

Then it can be shown that the differential equation (4.37) of second order converts to the system of two equations of the first order for $a(\tau)$ and $\theta(\tau)$:

$$\dot{a}(\tau) = -\frac{\varepsilon}{2} a(\tau) \sin(2\psi) \cos(\gamma\tau),$$
$$\dot{\theta}(\tau) = -\varepsilon \cos^2(\psi) \cos(\gamma\tau), \tag{4.41}$$

Where $\psi = \tau + \theta(\tau)$.

It is shown that the most intense parametric resonance and, therefore, maximal energy transfer to the system occurs, when the value of the frequency γ is close to the doubled frequency of free vibrations of the beam [49]. Consequently, we can set:

$$\gamma = 2 + \varepsilon\Delta. \tag{4.42}$$

The system of (4.41) can be written by introducing a new, slowly varying variable $\xi(\tau) = \gamma\tau - 2\psi$ as follows:

$$\dot{a}(\tau) = -\frac{\varepsilon}{2} a(\tau) \sin(2\psi) \cos(\xi(\tau) + 2\psi),$$
$$\dot{\xi}(\tau) = \varepsilon\Delta + 2\varepsilon \cos^2(\psi) \cos(\xi(\tau) + 2\psi). \tag{4.43}$$

Note that these equations are still exact, no averaging has been made as yet. Further on, the assumption for the value of the parameter ε is used: $0 < \varepsilon \ll 1$.

The method of averaging assumes that if $a(\tau)$ and $\xi(\tau)$ are smooth functions of the time such that their derivatives are small terms of order ε. Then values of these functions can be naturally seen as the superposition of slowly varying part and small rapidly oscillating terms. Considering these terms cause only small oscillations of a real function about its mean part, they can be neglected in zero-order approximation. Thus, the right-hand part of the previous system of equations (4.43) can be averaged on the variable ψ over one period:

$$\dot{a}_0(\tau) = \frac{1}{2\pi} \int_0^{2\pi} \dot{a}(\tau) d\psi = \frac{\varepsilon}{4} a_0(\tau) \sin(\xi_0(\tau)),$$
$$\dot{\xi}_0(\tau) = \frac{1}{2\pi} \int_0^{2\pi} \dot{\xi}(\tau) d\psi = \varepsilon\Delta + \frac{\varepsilon}{2} \cos(\xi_0(\tau)), \tag{4.44}$$

where $a_0 = a$ and $\xi_0 = \xi$ are held fixed during the integration. The system of differential equations (4.44) is nonlinear. However, it may be simplified to

a linear system with constant coefficients by defining new variables

$$\eta(\tau) = a_0(\tau)\cos\left(\frac{\xi_0(\tau)}{2} + \frac{\pi}{4}\right) \quad \text{and} \quad \zeta(\tau) = -a_0(\tau)\sin\left(\frac{\xi_0(\tau)}{2} + \frac{\pi}{4}\right) \tag{4.45}$$

Substituting $\eta(\tau)$ and $\zeta(\tau)$ into (4.44) gives:

$$\begin{aligned} \dot{\eta}(\tau) &= -\frac{\varepsilon}{4}\eta(\tau) + \frac{\varepsilon\Delta}{2}\zeta(\tau) \\ \dot{\zeta}(\tau) &= -\frac{\varepsilon\Delta}{2}\eta(\tau) + \frac{\varepsilon}{4}\zeta(\tau) \end{aligned} \tag{4.46}$$

The matrix corresponding to the system of constant coefficient linear differential equations (4.46) has the following eigenvalues

$$\lambda^2 = \frac{\varepsilon^2}{4}\left(\frac{1}{4} - \Delta^2\right). \tag{4.47}$$

According to Lyapunov stability theory [50], the solution of (4.46) is aperiodic and unstable, if an eigenvalue λ with positive real part exists. Thus, the resonance takes place within the interval

$$|\Delta| < \frac{1}{2} \tag{4.48}$$

around the frequency dimensionless value $\omega = 2$.

The range of parameters

$$0 < \varepsilon \ll 1 \quad \text{and} \quad |\gamma - 2| < \frac{\varepsilon}{2} \tag{4.49}$$

is called the region of the *principal parametric resonance*. The width of this region is proportional to the parameter ε [2].

Model 1 — Straight cylindrical beam (SCB)

For the SCB (Model 1), when $r_t = r_b$, the parameters defined by (4.38) are the following:

$$\delta = 1, \quad a_0 = \frac{1}{2}, \quad a_1 = \frac{\pi^4}{2}, \quad \tau = t\omega_0, \quad \gamma = \frac{\Omega}{\omega_0}, \quad \varepsilon = \frac{4L^2F_0}{\pi^3 E r_b^4}, \tag{4.50}$$

where $\omega_0 = \frac{\pi^2}{L^2}\sqrt{\frac{Er_b^2}{4\rho}}$ is the natural vibration frequency of the SCB (see (4.20)).

Thus, if $\varepsilon \ll 1$, the region of the principal parametric resonance of the SCB is

$$\sqrt{2 - \frac{\varepsilon}{2}}\,\omega_0 < \Omega < \sqrt{2 + \frac{\varepsilon}{2}}\,\omega_0. \tag{4.51}$$

Model 2 — Truncated conical beam (TCB)

For the special case of the TCB (Model 2), when $r_t = r_b/2$, the parameters (4.38) of the beam are

$$\delta = 0.5, \quad a_0 \approx 0.285, \quad a_1 \approx 16.761, \quad \tau = t\omega_0, \quad \gamma = \frac{\Omega}{\omega_0}, \quad \varepsilon \approx 0.375\frac{L^2 F_0}{E r_b^4},$$

where $\omega_0 \approx 3.832\dfrac{r_b}{L^2}\sqrt{\dfrac{E}{\rho}}$ (see (4.24)).

Thus, if $\varepsilon \ll 1$, the region of the principal parametric resonance of the TCB is

$$\sqrt{2 - \frac{\varepsilon}{2}}\,\omega_0 < \Omega < \sqrt{2 + \frac{\varepsilon}{2}}\,\omega_0. \tag{4.52}$$

5 Theoretical analysis of parametric vibrations of curved cylindrical beam

5.1 Formulation of the problem

In this chapter, parametric vibrations of a circular cylindrical beam (CCB) (Model 3) are analysed theoretically. According to [32], it is considered an Euler-Bernoulli beam whose underformed neutral axis is an arc of a circle with the radius R_0 and central angle $\pi/2 - \phi$ (Fig. 5.1). The diameter of the beam circular cross-section d is assumed to be constant along the axial direction. Herewith, the initial curvature of the beam is $\kappa_0 = -1/R_0 = \text{const}$.

The right-handed Cartesian coordinate system is placed such that the origin is in the middle of the base's cross-section, and the axial line of the beam lies in the x-y plane, which is the principal plane of the beam at each point. The circular axial line of the beam can be represented parametrically as $x = R_0(1 - \cos(s/R_0))$, $y = R_0 \sin(s/R_0))$, where $s \in [0, L]$ is the natural parameter, and $L = R_0(\pi/2 - \phi)$ is the length of the beam.

Consider the orthogonal basis vectors $\dot{e}_{i0}$, $i = 1, 2, 3$ attached to the axial line of the beam in the static equilibrium configuration, and the orthogonal basis $\dot{e}_i$, $i = 1, 2, 3$ to the moving curvilinear axial line of the beam (Fig. 5.1).

Cartesian basis vectors $\dot{e}_x, \dot{e}_y, \dot{e}_z$ are transformed to the attached basis $\dot{e}_{i0}$, $i = 1, 2, 3$ by the following matrix:

$$L^0 = (l^0_{ij}) = \begin{bmatrix} \cos\vartheta_{30}(s) & \sin\vartheta_{30}(s) & 0 \\ -\sin\vartheta_{30}(s) & \cos\vartheta_{30}(s) & 0 \\ 0 & 0 & 1 \end{bmatrix}, \tag{5.1}$$

where $\vartheta_{30}(s) = \pi/2 - s/R_0$ is the angle between the vectors $\dot{e}_{10}$ and $\dot{e}_x$, taken positive.

The periodic force $\dot{F}(t)$ applied directly toward the tip of the beam $s = L$ can be expressed as $\dot{F}(t) = -F_0 \cos(\Omega t)\dot{e}_1$, where F_0 is the constant amplitude and Ω is the constant angular frequency. We shall suppose throughout that vibrations of the beam caused by the force $\dot{F}(t)$ about its natural configuration in the x-y plane are *small*. That means that the displacement vector $\dot{u}(s, t)$ and the angle $\vartheta_3(s, t)$ between vectors $\dot{e}_1$ and $\dot{e}_{10}$ are of the first order of smallest(see Fig. 5.1(a)). It will be also assumed that ϕ is a small angle in order to show analytical methods in detail for the slightly simpler case. Cartesian basis vectors $\dot{e}_x, \dot{e}_y, \dot{e}_z$ can be transformed to the attached basis

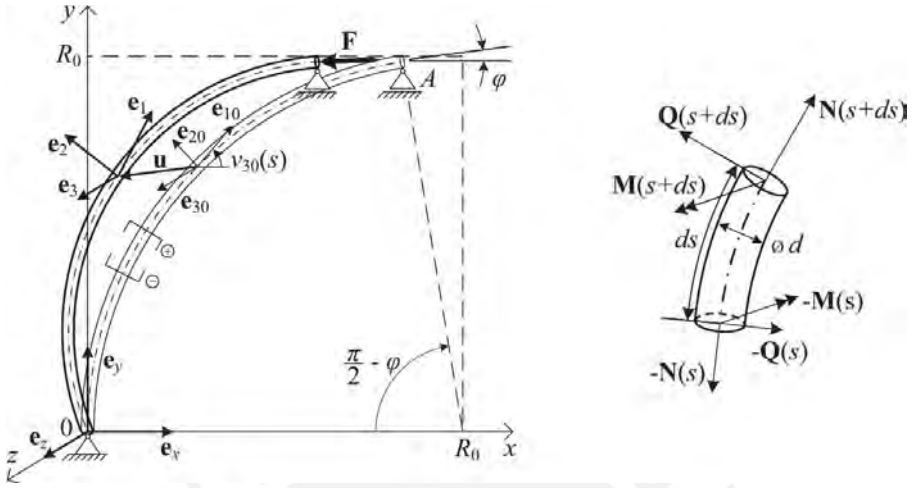

Figure 5.1: (a) Deflection of the CCB under the force acting on the tip. (b) Free-body diagram of a beam element of infinitesimal length ds with internal actions upon it [32]

$\dot{e}_i$, $i = 1, 2, 3$ as follows:

$$\dot{e}_i = l_{ij} l^0_{j\kappa} \dot{e}_k, \quad \text{where} \quad L = (l_{ij}) = \begin{pmatrix} 1 & \vartheta_3(s,t) & 0 \\ -\vartheta_3(s,t) & 1 & 0 \\ 0 & 0 & 1 \end{pmatrix}. \qquad (5.2)$$

Here, the summation on repeating indexes $j = 1, 2, 3$ and $k = x, y, z$ is meant.

In the attached coordinate system $\dot{e}_i$, $i = 1, 2, 3$, the displacement vector $\dot{u}$ of the beam axis points has two time-dependent components:

$$\dot{u} = u_1(s, t)\dot{e}_1 + u_2(s, t)\dot{e}_2. \qquad (5.3)$$

Small deflection theory, together with the assumption of an inextensible axial line, shows that the change in curvature $\Delta\kappa = \kappa - \kappa_0$ and the local transverse displacement $u_2(s, t)$ are related through

$$\Delta\kappa = \kappa_0 u_2 + \frac{\partial^2 u_2}{\partial s^2}, \quad \text{where} \quad \kappa_0 = -\frac{1}{R^0}. \qquad (5.4)$$

This means that the change in curvature is of first-order smallness.

5.2 Governing equation of the curved beam and its approximation

According to [32], differential equation that represents the in-plane vibrational motion of the CCB is derived from consideration of the variation of forces and moments across an element of the beam. Consider the free-body diagram of an element of the beam shown in (Fig. 5.1(b)), where $\dot{N} = N(s, t)\dot{e}_1$ is the normal axial force, $\dot{Q} = Q(s, t)\dot{e}_2$ is the transverse shear force, and $\dot{M} = M(s, t)\dot{e}_3$ is the bending moment.

For the circular beam with constant initial curvature, the in-plane vibrational motion of the beam can be described with a single partial differential equation of sixth order. With regard to the rotary inertia and in the absence of the force of viscous damping, the equation of motion in terms of $u_2(s, t)$ has the following form [46]:

$$L(u_2) = 0, \tag{5.5}$$

where

$$L(u_2) = \rho A \frac{\partial^2 u_2}{\partial t^2} - \frac{\rho A}{\kappa_0^2}\frac{\partial^4 u_2}{\partial s^2 \partial t^2} + \rho I_z \frac{\partial^2}{\partial t^2}\left(\frac{1}{\kappa_0^2}\frac{\partial^4 u_2}{\partial s^4} + 2\frac{\partial^2 u_2}{\partial s^2} + \kappa_0 u_2^2\right)$$
$$- EI_z\left(\frac{1}{\kappa_0^2}\frac{\partial^6 u_2}{\partial s^6} + 2\frac{\partial^4 u_2}{\partial s^4} + \kappa_0\frac{\partial^2 u_2}{\partial s^2}\right) + \frac{1}{\kappa_0^2}\frac{\partial^2}{\partial s^2}\left(N(s, t)\left(\frac{\partial^2 u_2}{\partial s^2} + \kappa_0 u_2\right)\right)$$
$$+ \frac{1}{\kappa_0}\frac{\partial}{\partial s}\left(Q(s, t)\left(\frac{\partial^2 u_2}{\partial s^2} + \kappa_0 u_2^2\right)\right).$$

Here, ρ is the mass density of the beam material, $A = \pi d^2/4$ is the cross-sectional area, d is the diameter of the beam, $I_z = \pi d^4/64$ is the moment of inertia of the cross-section, and $E = \text{const}$ is Young's modulus.

The components of the normal force $\dot{N} = N(s, t)\dot{e}_1$ and the shear force $\dot{Q} = Q(s, t)\dot{e}_2$ are

$$N(s, t) = F(t)[(\cos(\phi)\sin(\kappa_0 s) - (1 + \sin(\phi))\cos(\kappa_0 s)]$$
$$Q(s, t) = F(t)[\cos(\phi)\cos(\kappa_0 s) + (1 + \sin(\phi))\sin(\kappa_0 s)]. \tag{5.6}$$

The bending moment $\dot{M} = M(s, t)\dot{e}_3$ at any cross-section of the beam can be expressed in terms of displacement component $u_2(s, t)$ as

$$M(s, t) = EI_z\Delta\kappa = EI_z\left(\kappa_0^2 u_2 + \frac{\partial^2 u_2}{\partial s^2}\right). \tag{5.7}$$

At the pinned left end of the beam $s = 0$ there cannot be any displacements or bending moment. At the right end of the beam the support allows small displacement only in the horizontal direction. That means the y-coordinate of $\vec{u}$ is zero. Using equations (5.2) and (5.3) and retaining linear terms, we get $u_2 = 0$ at $s = L$. Since no external bending moment is applied at the right end of the beam, the bending moment at that location is zero. Consequently, we have the following boundary conditions for the function $u_2(s, t)$ itself as well as for the second derivative of it:

$$u_2(0, t) = u_2(L, t) = 0 \quad \text{and} \quad \frac{\partial^2 u_2(s,t)}{\partial s^2}\Big|_{(0,t)} = \frac{\partial^2 u_2(s,t)}{\partial s^2}\Big|_{(L,t)} = 0. \qquad (5.8)$$

Just like in chapter 4.6, it is assumed a one-term approximation by Galerkin's Method of (5.5) in the form $\tilde{u}_2(s, t) = \sin(\pi s/L) f(t)$, which satisfies the support boundary conditions of the beam (5.8). Substituting this expression for $\tilde{u}_2(s, t)$ in equation (5.5), we obtain a second-order ordinary differential equation for the function $f(t)$. It can be written in the dimensionless form as

$$\ddot{f}(\tau) + (1 - \varepsilon\cos(\gamma\tau))f(\tau) = 0, \qquad (5.9)$$

Here, dimensionless variables are introduced as second-order approximation with respect to the small angle parameter ϕ:

$$\tau = \frac{t}{t_c}, \quad \gamma = \Omega t_c, \quad \varepsilon = \frac{512 R_0^2 F_0}{5\pi^2 E d^4}\left(1 - \frac{182}{45\pi}\phi - \left(\frac{1}{2} - \frac{2036}{225\pi^2}\right)\phi^2\right), \qquad (5.10)$$

where

$$t_c = \frac{R_0}{6d}\sqrt{\frac{\rho}{E}(80R^2 + 9d^2)}\left(1 - \frac{2(688R_0^2 + 27d^2)}{3\pi(80R_0^2 + 9d^2)}\phi + \frac{128R_0^2(6704R_0^2 + 1107d^2)}{9\pi^2(80R_0^2 + 9d^2)^2}\phi^2\right). \qquad (5.11)$$

5.3 The principle range of the parametric resonance

Equation (5.9) is the second-order linear ordinary differential equation with periodic coefficient. So, parametric vibrations of the beam with constant

initial curvature can be described by the same Mathieu equation (see (3.12) and (4.37). The parameter ε can be treated as a small parameter: $\varepsilon \quad 1$.

It is shown theoretically in chapter 4.7 that the principle parametric resonance of the beam (CCB) occurs for infinite number of excitation angular frequency values Ω, see (5.10), and the principle range of the parametric resonance, as seen in (4.49):

$$2 - \frac{\varepsilon}{2} < \Omega t_c < 2 + \frac{\varepsilon}{2}. \tag{5.12}$$

6 Numerical simulations

The response of the parametrical excitation in our analysis (Model 1 to Model 3), corresponds to the nonlinear behaviour of the displacements. Studies of phase difference between input and response are also performed for the transient responses for a range of excitation frequencies. This phenomenon is described by (4.33, 5.5), depending on the geometrical model to be analysed. These models are described by partial differential equations (PDEs). The solution of the PDEs with respect to the boundary conditions has to be obtained using numerical methods. A commonly used numerical approximation of structural mechanic problems is the finite element method (FEM). The basic functional principle of the FEM is to discretize a large domain with small elements, at which a local shape function is used to match the underlying PDE. The quality of the FEM-approximation works best, if a large number of elements is used. For multi-dimentional problems, e.g. the approximation of shells or volumes, the geometry of each element should match the used shape function. Keeping these fundamentals in mind, the FEM is able to handle complicated geometries, different material characteristics and a variety of accuracy.

With the advances in the commercial finite element codes and numerical integration methods, it is possible to compute geometrical nonlinearities and other nonlinear effects in structural behavior. In this analysis, the transient response of our models is simulated for a periodic excitation with initial condition and without damping using the capabilities of the FEM software ANSYS.

6.1 Remarks on FEM

According to [51], for most structural dynamic problems of a mechanical system, the spatial concretization for the principle of virtual work using the finite element method gives the finite element semi-discrete equation of motion as follows:

$$[M]\{\ddot{u}(t)\} + [C]\{\dot{u}(t)\} + \{F^i(t)\} = \{F^a(t)\} \tag{6.1}$$

where $[M]$ is the structural mass matrix, $[C]$ is the structural damping matrix, $\{\ddot{u}(t)\}$ is the nodal acceleration vector, $\{\dot{u}\}$ is the nodal velocity vector, $\{u(t)\}$ is the nodal displacement vector, $\{F^i(t)\}$ is the internal load vector, $\{F^a(t)\}$ is the applied load vector.

The structural dynamics problems concerned with the mechanical behavior governed by the above differential equation can be classified into two classes; that is, linear and nonlinear problems. In linear structural dynamics systems, the internal load is linearly proportional to the nodal displacement, and the structural stiffness matrix remains constant. Therefore, equation 6.1 can be rewritten as:

$$[M]\{\ddot{u}(t)\} + [C]\{\dot{u}(t)\} + [K]\{\dot{u}(t)\} = \{F^a(t)\} \tag{6.2}$$

where $[K]$ is the structural stiffness matrix. In nonlinear structural dynamics problems, the internal load is no longer linearly proportional to the nodal displacement, and the structural stiffness matrix is dependent on the current displacement ($[K\{u\}]$).

Three methods are available for solving equation 6.2:

- Central difference time integration method: used for explicit transient analyses.
- Newmark time integration method: used for implicit transient analyses.
- Hilber-Hughes-Taylor (HHT) time integration method: used also for implicit transient analyses, this method is an extension of the Newmark time integration method.

For a nonlinear system, a linearized form of the time integration methods can be obtained by the Newton-Raphson method, see [51].
The Models (1 through 3) were made in ANSYS 16.2 and the used module was Workbench Mechanical which is used to develop transient analysis, linear and nonlinear.

According to Ansys's guidelines, there are different types of elements available for use in our analysis, we will use elements of type BEAM (one dimensional geometries) and SOLID (three dimensional geometries) because BEAM elements fit best to the geometry of the problem, but SOLID elements do not require an a-priori estimation of effects like shearing. The obious downside of using solid elements is the large equation system, which inevitable results. The characteristic and behaviour of the element will be described in the following cited.

According to [51]:

Beam3: The element is based on Euler-Bernoulli beam theory, which is considered an uniaxial element with tension, compression, and bending capabilities. The element has three DOF at each node: translations in the nodal x and y directions and rotation about the nodal z-axis.

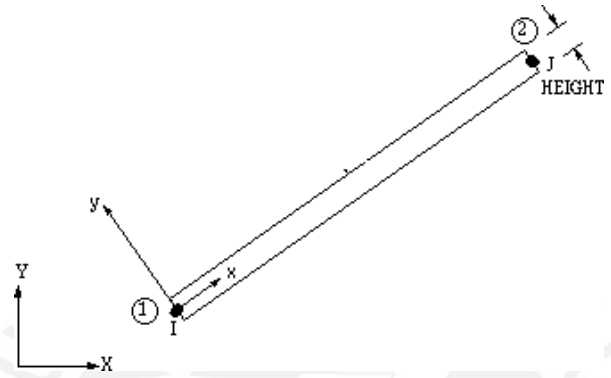

Figure 6.1: Beam3: 2D-element with 3 DOF at each node [51]

Beam188: The element is based on Timoshenko beam theory which includes shear-deformation effects. The element has six DOF at each node, these include translations in the x, y, and z directions and rotations about the x, y, and z directions. This element is well-suited for linear, large rotation, and/or large strain nonlinear applications.

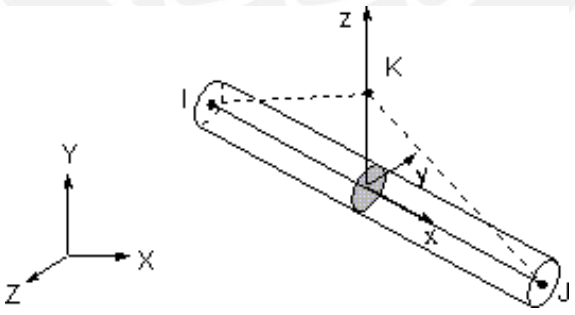

Figure 6.2: Beam188: 3D-element with 6 DOF at each node [51]

SOLID186: Is a higher order 3-D 20-node solid element that exhibits quadratic displacement behaviour. The element is defined by 20 nodes hav-

ing three degrees of freedom per node: translations in the nodal x, y, and z directions. The element supports plasticity, hyperelasticity, creep, stress stiffening, large deflection, and large strain capabilities.

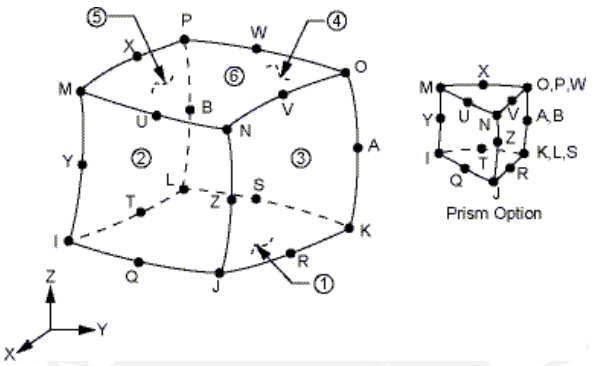

Figure 6.3: Beam186: 3D-element with 6 DOF at each node [51]

Loads: It is important to note the orientation of loads and its effect on the structure in large-deflection analyses. The pressure remains always perpendicular to the surface, than the force load and moment load, which remains with constant direction.

6.2 Simulation for Model 1 – Straight cylindrical beam (SCB)

6.2.1 Geometry and properties of the model

An SCB (Model 1) is modeled in ANSYS 16.2 Workbench as a straight line body. The geometrical characteristics of the model are the length L and the radius r_b. The material parameters are the density ρ and the Young's modulus E. The values of the parameters are given in table 1. As it will be shown below, these values are choose in such a way that the first natural vibration frequency of the SCB $\omega_0 \approx 1$ Hz holds for the theoretical model introduced in chapter 4. This allows a reasonable adequate time step size in the numerical simulation. No damping is considered.

According to the theoretical model in the chapter 4, the periodic force perpendicular to the cross-section at the tip of the beam is applied (Fig. 4.1). Since it is not possible to apply a following force to the cross-section of the line body, it is necessary to define a solid body — a circular cylinder, which

Table 1: Properties of the model 1 of the SCB

MODEL 1		
	Line Body	Solid body
L (mm)	50	1
r_b (mm)	1	1
ρ (kg/m^3)	1000	1e-6
E (N/m^2)	10313	2e+13

is attached to the line body. The parameters of the cylinder are listed in table 1. The cylinder can be considered massless, since the mass of it is defined to be small (close to zero). Figure 6.4 shows the geometry of the model.

According to [51], a line body with beam elements (beam3, beam44, beam188, etc.) has less number of elements than a body meshed with solid elements. This is important for computing resources and the duration of a simulation. Also, the meshing of the model needs to correspond to the nonlinear behaviour and its symmetry.

In the present numerical simulation for the Model 1, the beam element (beam188) is used for the line body, and the solid element (solid186) is used for the cylinder (Fig. 6.4, right). The number of elements of the line body is

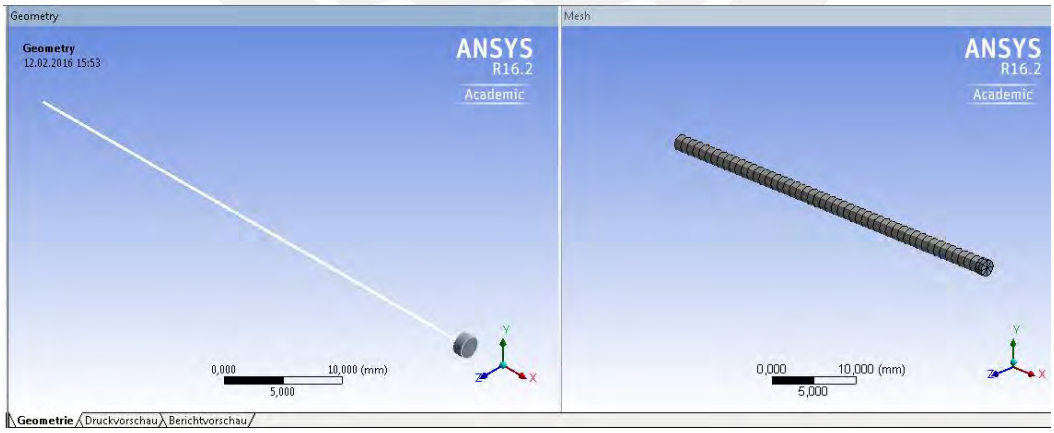

Figure 6.4: (a) Geometry of the Model 1; (b) Meshing of the Model 1 with beam and solid elements

50 and of the solid cylinder is 16. The total number of nodes is 194.

The transition between elements of the line and solid bodies is defined with the bonded type of contact. The multi-point constraint bonded contact (MPC) is used to consider the effects of the large-deformation, see Fig. 6.5. Both translational and rotational degrees of freedom are accounted for.

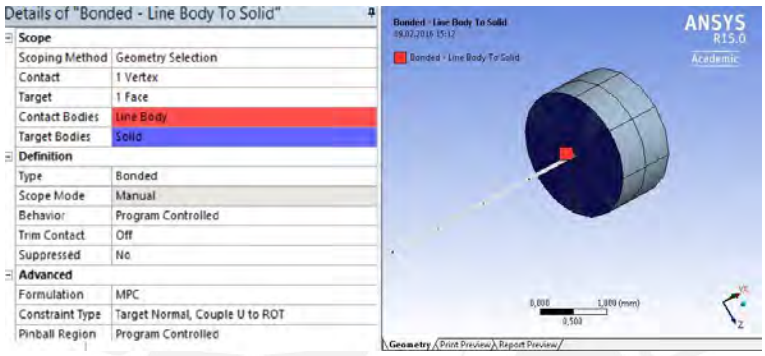

Figure 6.5: MPC-based bonded contact between the line and solid bodies

The corresponding pinned–pinned boundary conditions for the model are applied according the theoretical formulation of the problem (see Fig. 4.1 and (4.34)). The left end point of the line body is pinned. It means that there is no displacement in all three directions and the rotation only around the z axis is free. The left cross-section of the solid body (cylinder) is pinned with free displacement along the x axis and free rotation around the z axis.

In the model, the damping is not consider. The numerical damping is defined manually to be equal zero.

6.2.2 Modal analysis of the natural vibration frequencies

This chapter contains numerical results of the natural vibration frequencies of the SCB for the parameters listed in table 1. The results are compared with the values given by the theoretical formula (4.20) for the Euler-Bernoulli beam.

The numerical analysis is done in ANSYS 16.2 Workbench using analysis system "Modal". The modal analysis determines the vibration characteristics (natural frequencies and mode shapes) of a structure or a particular component.

In order to compare the influences of the different meshing elements on the numerical values of the natural frequencies, simulations with the following elements are made: beam3, beam188, and solid186.

Table 2 shows the theoretical and numerical results of the first three transverse natural frequencies of the SCB for the chosen values of the parameters (see table 1). It maybe seen that the numerical results for all used types of finite elements are close to the theoretical values. However, the solid model has 512 solid elements and 2201 nodes. Line body models with beam3 or beam188 have 66 elements and 194 nodes. That is why based on these results, the element type beam188 further on will be used in numerical analysis of the parametrical resonance.

The corresponding theoretical mode shapes of transverse vibrations of the SCB are evaluated according to (4.21) and presented in Fig. 4.3. The mode shapes of the SCB obtained numerically for the beam188 elements in ANSYS 16.2 Workbench are shown in Fig. 6.6.

Table 2: Comparison of the theoretical and numerical results for the natural vibration frequency of the SCB (Model 1) in Hz.

Modal Analysis				
	Theory	Numerical calculation with ANSYS		
	Euler-Bernoulli	Beam3	Beam188	Solid model
ω_1	1.0089	1.0070	1.0068	1.0053
ω_2	4.0355	4.0080	4.0070	4.0016
ω_3	9.0800	8.9526	8.9439	8.9324
		66 Elements		512 Elements
		194 Nodes		2201 Nodes

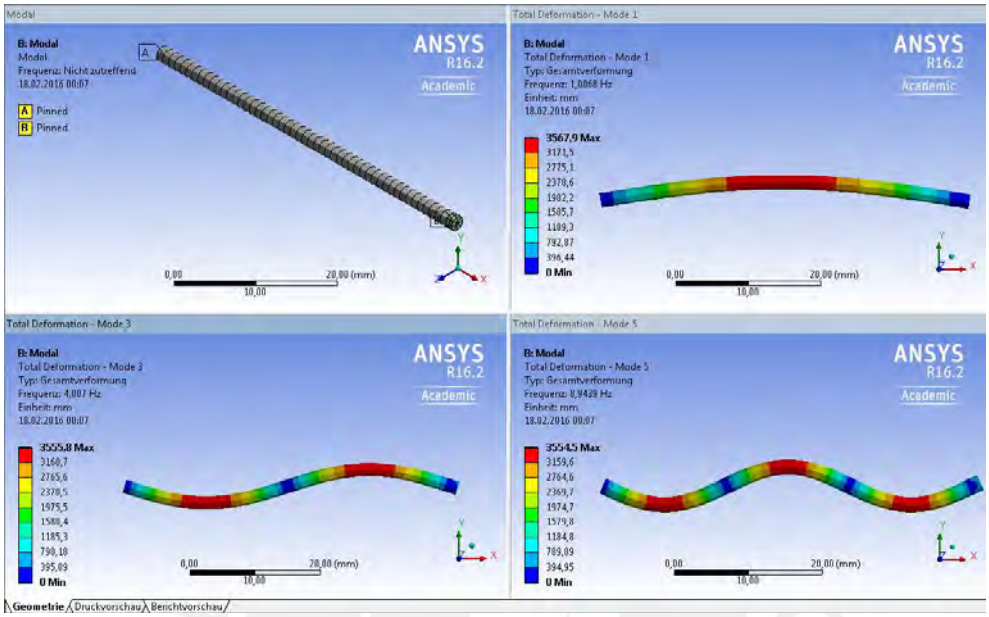

Figure 6.6: Mode shapes of transverse vibrations of the SCB

6.2.3 Transient analysis of the parametric excited SCB

In ANSYS, the analysis system ”Transient structural” is used to determine the dynamic response of a structure under the action of any general time-dependent loads. It can be used to determine time-varying displacements in a structure as it responds to any transient loads. The effects of the inertia and damping maybe considered important in this analysis.

According to the previous section, the line body is meshed by beam elements (beam188) to evaluate the transient analysis. The boundary conditions are chosen according to the theoretical model in chapter 4.6. The left end point of the line body is pinned. It means that there is no displacement in all three directions and the rotation only around the z axis is free. The left cross-section of the solid body (cylinder) is pinned with free displacement along the x axis and free rotation around the z axis, see Fig. 6.7.

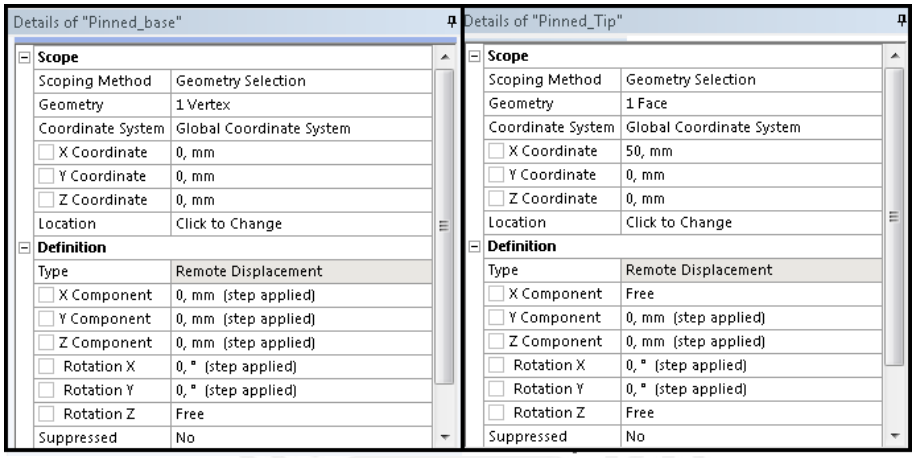

Figure 6.7: Boundary conditions at the base and at the tip of the model

The time-varying load is defined as a periodic following pressure $P(t) = -P_0 \cos(\Omega t)$ normal to the cross-section of the cylindrical solid body. The amplitude of the pressure is P_0 = 3 Pa. Thus, the periodic following force acting on the system is $\dot{F}(t) = \pi r_b^2 P(t)\dot{n}_t$, where $\dot{n}_t$ is the normal vector to the cross-section. Note that the replacement of the normal force with pressure is necessary to define a load in the normal direction to the cross-section of the deformable beam.

As it was shown before, the transient analysis of parametric excited vibrations requires an initial deflection of the system from the equilibrium position. That is why, an additional load is needed to establish an initial displacement u_0 and an initial velocity $\dot{u}_0$ of the system.

The applying load process in the model is developed in three steps. The first dynamic load (the force $\dot{F}_0$) is applied linearly at the middle of the line body in the y direction within a time range [0, 0.25] s and discharged linearly within a time range [0.25, 0.5] s. The maximum value of the force is $F_0 = 10^{-7}$ N. These are the load steps 1 and 2, during which the initial deflection of the beam occurs. These time ranges are chosen according to the period of the time-varying pressure load $P(t)$ as $0.25 \approx \pi/\Omega$ and $0.5 \approx 2\pi/\Omega$. The third main load step is within a time range [0.25, 30] s. The periodic excitation load $P(t)$ is applied during load steps 2 and 3. The configuration of loads and boundary conditions of the Model 1 at the instant 0.25 s is shown in the Fig. 6.8. The sequence of the three load steps of the model is presented in the Fig. 6.9.

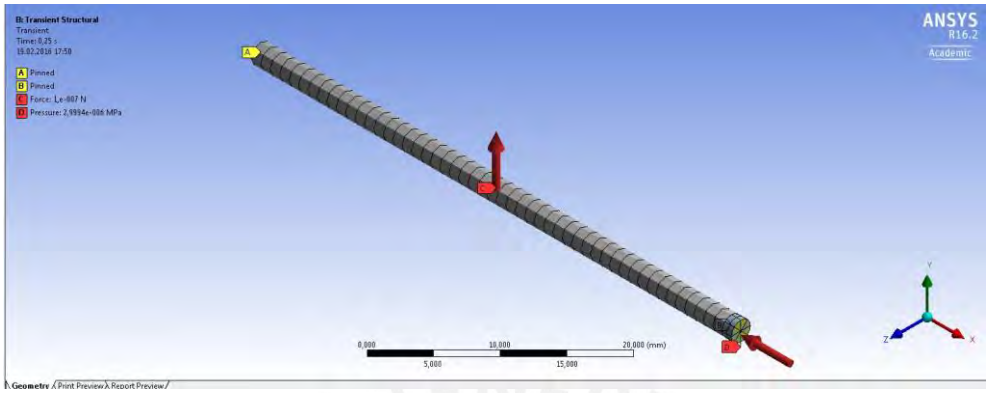

Figure 6.8: Model 1 of the parametrically excited SCB

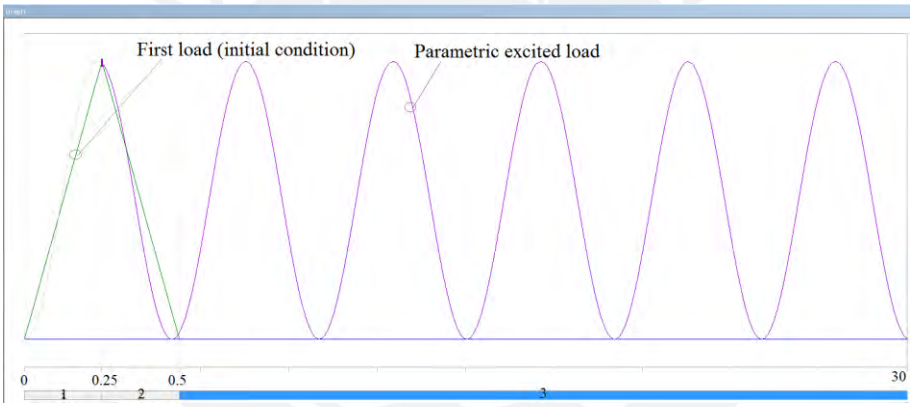

Figure 6.9: Three load steps of the Model 1: 1) [0, 0.25] s; 2) [0.25, 0.5] s; 3) [0.5, 30] s

Each dynamic load is established with a time integration, called time step, enough small to capture the response of the system. The time step is defined considering the maximal ideal time point per cycle $\Delta t = 1/(20\nu)$, where the frequency $\nu = \Omega/(2\pi)$ is measured in Hz (see Fig. 6.10).

Step Controls	
Number Of Steps	3,
Current Step Number	3,
Step End Time	30, s
Auto Time Stepping	On
Define By	Time
Carry Over Time Step	Off
Initial Time Step	1,e-002 s
Minimum Time Step	1,e-003 s
Maximum Time Step	1,e-002 s
Time Integration	On

Figure 6.10: Settings of the load step 3, during which the parametrical excitation is applied

Simulation results

As it is shown theoretically in chapter 4.7, the most response of the system on the parametrical excitation occurs close to the doubled first natural frequency of the system (see (4.49)). This range is called *the region of the principal parametric resonance*. The numerical simulations of the transient analysis are made for the excitation frequencies $\Omega \approx 2\omega_0$ in order to find this principal range and also for $\Omega \approx \omega_0$ in order to find the second range of the parametric resonance.

The results of simulations show that the Model 1 of the SCB exhibits parametrical resonance vibrations within the following ranges of the excitation frequency $\nu = \Omega/(2\pi)$:

the principal range of the parametric resonance:

$$1.87 \text{ ™ } \nu \text{ ™ } 2.15 \text{ Hz};$$

the second range of the parametric resonance:

$$0.99 \text{ ™ } \nu \text{ ™} 1.01 \text{ Hz}. \quad (6.3)$$

According to chapter 4.7, for the chosen values of the simulation parameters the first natural vibration frequency of the SCB is $\omega_0 = 1.0089$ Hz and the dimensionless parameter $\varepsilon = 0.2947$, see (4.50). As it was shown before, the theoretical region of the principal parametric resonance depends on ε and ω_0 and it is within a range (4.51):

$1.8691 < \nu < 2.1665$ Hz.

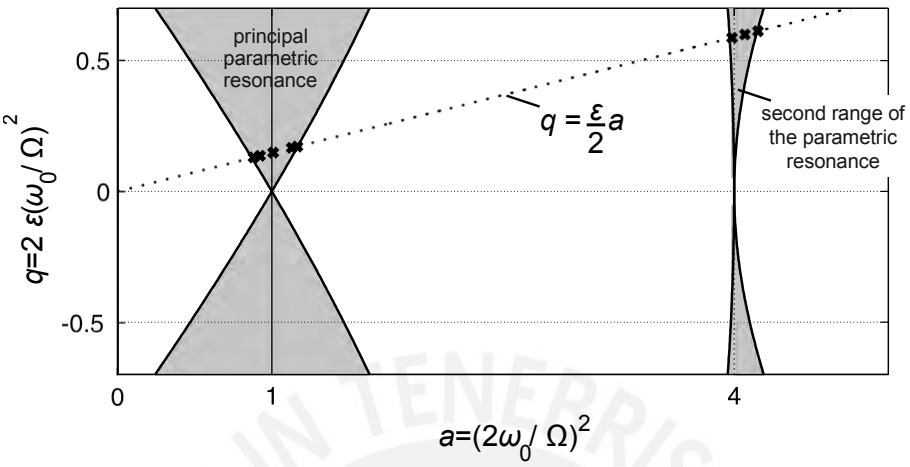

Figure 6.11: Ince-Strutt diagram of the Mathieu equation (4.37) indicating the theoretical transition curves, which divide the a-q plane in stable (white) and unstable (grey) regions. Cross markers ($\times$) correspond to the values of Ω, for which it is shown numerically that the parametric resonance takes place. $\omega_0 = 1.0089$ Hz and $\varepsilon = 0.2947$

Figure 6.11 shows the Ince-Strutt diagram of the Mathieu equation (4.37). Theoretical transition curves divide the plane of the parameters $a = (2\omega_0/\Omega)^2$ and $q = 2\varepsilon(\omega_0/\Omega)^2$ in stable and unstable regions. The range close to $a \approx 1$, i.e. $\Omega \approx 2\omega_0$, is the region of the principal parametric resonance. The range close to $a \approx 4$, i.e. $\Omega \approx \omega_0$, is the second range of the parametric resonance. For $\omega_0 = 1.0089$ Hz and $\varepsilon = 0.2947$, the results of the numerical simulation (6.3), for which the parametric resonance takes place, are indicated with cross markers ($\times$). It maybe seen that theoretical and numerical results correspond to each other.

For example, for the excitation frequency $\nu = 2.01$ Hz, which is within the region of the principal parametric resonance (6.3), the transverse displacement of the cross-section of the SCB at $x = L/2$ is presented in Fig. 6.12. It is obvious that the parametric resonance takes place, and the amplitude of the vibrations increases exponentially with time. Moreover, this result is compared with the conclusions of the theoretical analysis. The averaged amplitude $a_0(t)$ of parametric vibrations, calculated according to the analysis in chapter 4.7, is plotted for the initial amplitude value $a_0(0) = 0.024$ mm.

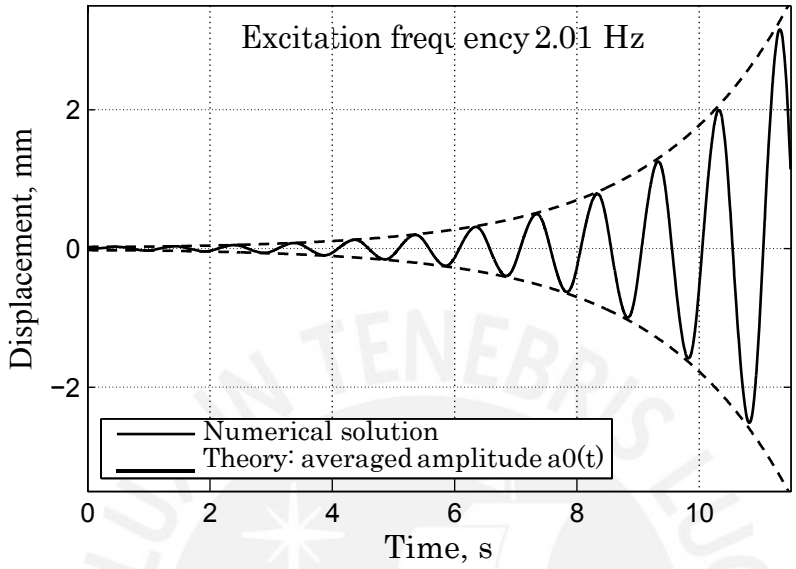

Figure 6.12: Transverse displacement of the cross-section of the SCB at $x = L/2$ for the excitation frequency ν = 2.01 Hz, ω_0 = 1.0089 Hz and ε = 0.2947. Solid line – the result of the numerical simulations; dashed line – the averaged amplitude $a_0(t)$ obtained theoretically for $a_0(0)$ = 0.024 mm

Figure 6.13 shows the steady-state response of the system to the excitation frequency ν = 2.17 Hz, which is outside of the region of the principal parametric resonance (6.3), i.e. it corresponds to the region of stability. The transverse displacement of the cross-section of the SCB at $x = L/2$ is plotted as a function of time. Furthermore, the averaged amplitude $a_0(t)$ of parametric vibrations, calculated according to the theoretical analysis in chapter 4.7, is plotted for the initial amplitude value $a_0(0)$ = 0.0265 mm and $\theta(0)$ = 1.4573 . It may be see that the amplitude remains small and limited with time. The graph resembles the diagram of beat frequency in acoustic.

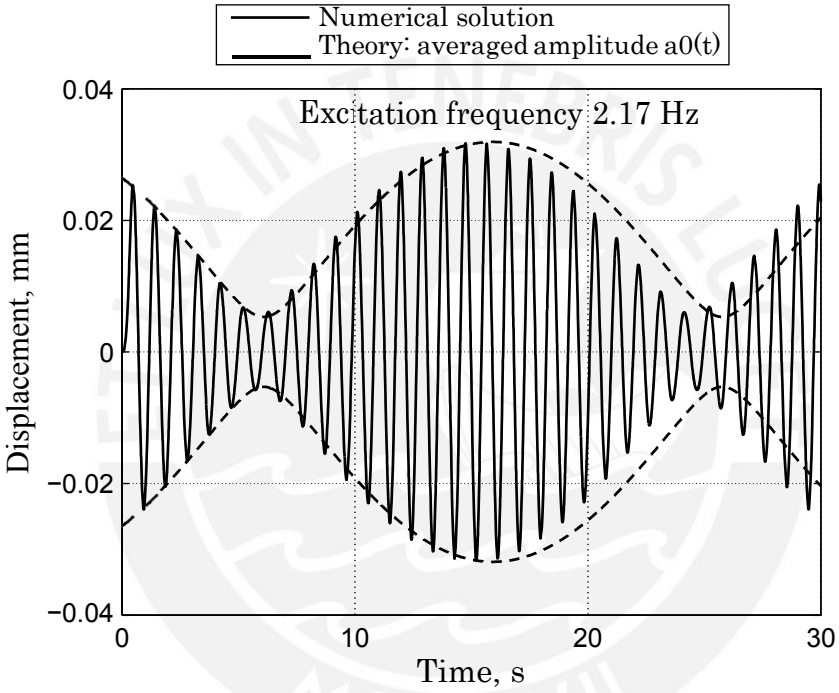

Figure 6.13: Transverse displacement of the cross-section of the SCB at $x = L/2$ for the excitation frequency $\nu = 2.17$ Hz, $\omega_0 = 1.0089$ Hz and $\varepsilon = 0.2947$. Solid line – the result of the numerical simulations; dashed line – the averaged amplitude $a_0(t)$ obtained theoretically for $a_0(0) = 0.0265$ mm and $\theta(0) = 1.4573$

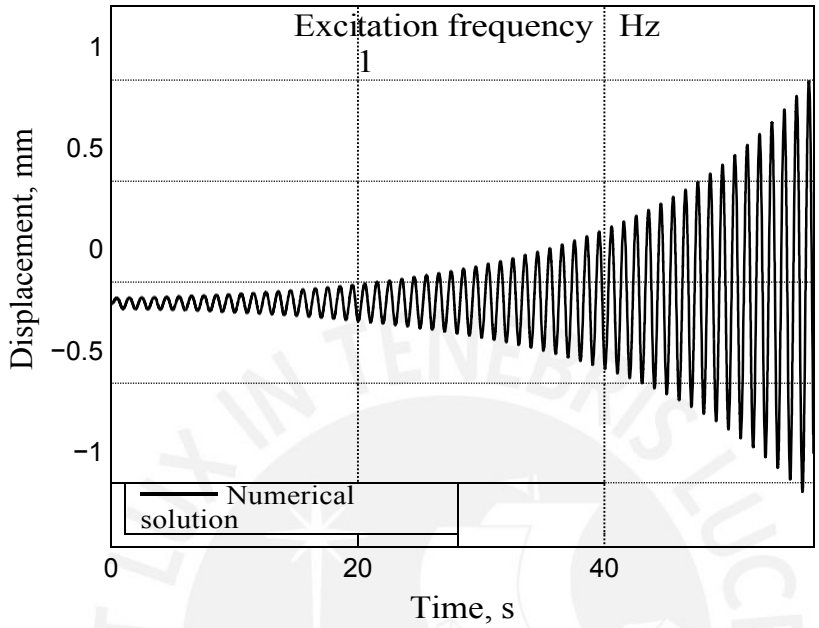

Figure 6.14: The second region of the parametric resonance: transverse displacement of the cross-section of the SCB at $x = L/2$ for the excitation frequency $\nu = 1.0$ Hz, $\omega_0 = 1.0089$ Hz and $\varepsilon = 0.2947$

Considering an excitation frequency $\nu = 1.0$ Hz, which is within the second region of the parametric resonance (6.3), the transverse displacement of the cross-section of the SCB at $x = L/2$ is presented in Fig. 6.14. It is obvious that the parametric resonance takes place, and the amplitude of the vibrations also increases exponentially with time. The theoretical analysis for the second region is out of the scope of the present thesis.

As it may be seen qualitatively in Fig.6.12 and 6.14, the response of the system on the parametrical excitation is stronger within the range of the principal parametrical resonance than within the second range.

Figure 6.15 shows the steady state response of the system to the frequency $\nu = 1.03$ Hz, which is outside of the region of the second parametric resonance (6.3). It shows the transverse displacement of the cross-section of the SCB at $x = L/2$ depending on the time.

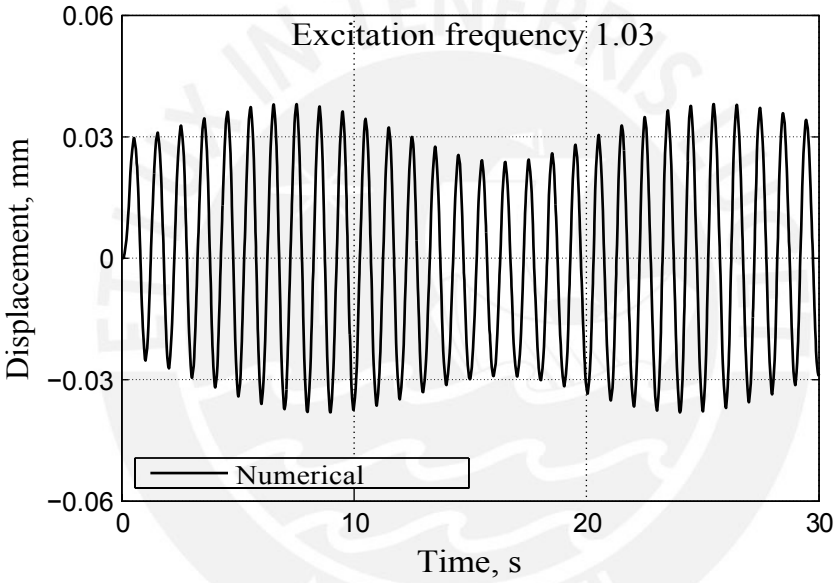

Figure 6.15: Transverse displacement of the cross-section of the SCB at $x = L/2$ for the excitation frequency ν = 1.03 Hz, ω_0 = 1.0089 Hz and ε = 0.2947

6.3 Simulation for Model 2 –Truncated conical beam (TCB)

6.3.1 Geometry and properties of the model

An TCB (Model 2) is modeled in ANSYS 16.2 Workbench as a straight solid body. The model has a variable circular cross-section. The radius of the cross-section develops linearly along the axial direction of the TCB $r(x) = r_b + (r_t - r_b)x/L$, where r_b and r_t are the radii at the base and the tip of the beam, respectively (Fig. 4.1). The material parameters, the density ρ and the Young's modulus E, are same as for the SCB (Model 1). The values of the parameters are given in table 3.

In the present numerical simulation for the Model 2, the solid element (solid186) is used. The number of elements of the solid body is 504. The total number of nodes is 2167 (Fig. 6.16).

The corresponding pinned-pinned boundary conditions for the model are applied similarly as for the Model 1. The left end cross-section of the solid body is pinned. It means that there is no displacement in all three directions and the rotation only around the z axis is free. The right cross-section is pinned with free displacement along the x axis and free rotation around the z axis. In the model, the damping is not consider. The numerical damping is defined manually to be equal zero.

Table 3: Properties of the Model 2 of the TCB

MODEL 2	
	Solid Body
L (mm)	50
r_b (mm)	1
r_t (mm)	0.5
ρ (kg/m^3)	1000
E (N/m^2)	10313

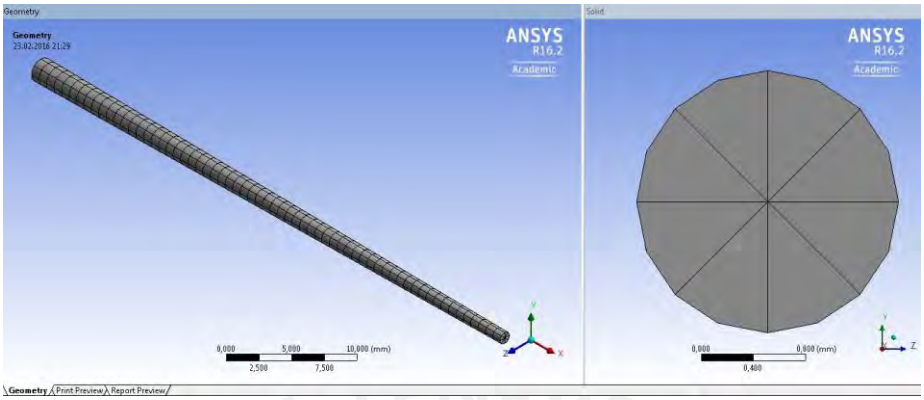

Figure 6.16: (a) Geometry and meshing of the Model 2; (b) Cross-section of the Model 2

6.3.2 Modal analysis of the natural vibration frequencies

This chapter contains numerical results of the natural vibration frequencies of the TCB for the parameters listed in table 3.

The theoretical value of the first natural vibration frequency of the TCB is given by the formula (4.24) based on the Rayleigh's method. Table 4 shows the theoretical and numerical results of the first three transverse natural frequencies of the TCB. It maybe seen that the value of the first natural frequency obtained numerically is slightly lower than the theoretical value. Thus, this corresponds to the fact that the Rayleigh's quotient gives the upper boundary value for the first eigenfrequency.

The mode shapes of the TCB obtained numerically for the solid168 ele-

Table 4: Natural vibration frequencies of the TCB (Model 2) in Hz

Modal Analysis		
	Theory	Numerical
ω_1	0.7869	0.7090
ω_2		2.9593
ω_3		6.6026
		504 Elements
		2167 Nodes

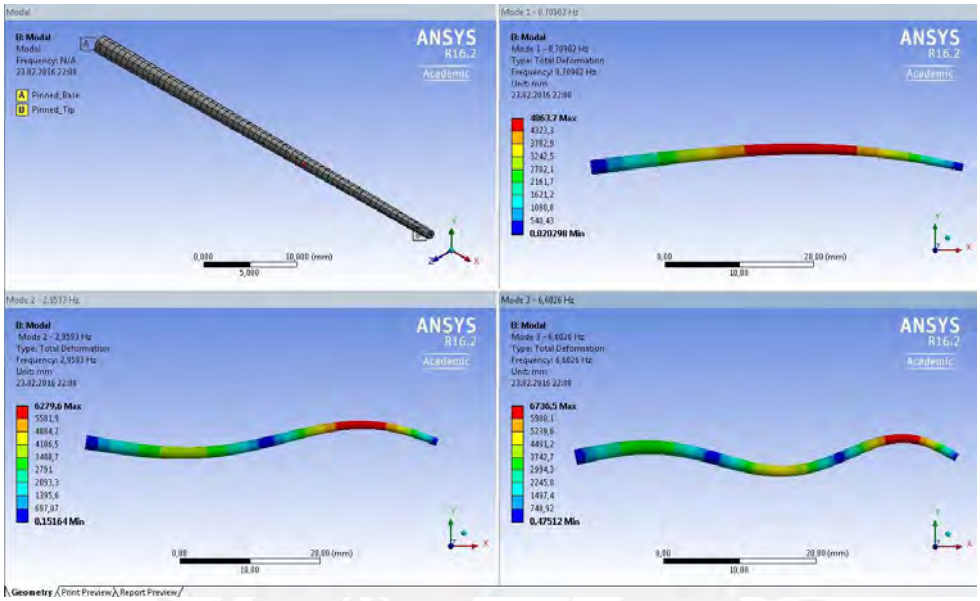

Figure 6.17: Mode shapes of transverse vibrations of the TCB

ments in ANSYS 16.2 Workbench are shown in Fig. 6.17.

6.3.3 Transient analysis of the parametric excited TCB

The response of the TCB on the parametric excitation is simulated in the analysis system "Transient structural", ANSYS 16.2 Workbench, in the same manner as for the SCB in section 6.2.3. The solid body is meshed by solid186 elements to evaluate the transient analysis. The boundary conditions are chosen according to the theoretical model in chapter 4, see Fig. 6.18.

The time-varying load is defined as a periodic following pressure $P(t) = -P_0 \cos(\Omega t)$ normal to the cross-section of the solid body. The amplitude of the pressure is P_0 = 3 Pa. Thus, the periodic force acting on the system is $\dot{F}(t) = \pi r_t^2 P(t) \dot{n}_t$, where $\dot{n}_t$ is the normal vector to the cross-section. Note that the replacement of the normal force with pressure is necessary to ensure a load in direction of the normal cross-section of the deformed beam.

The applying load process in the model is developed in three steps. To create an initial displacement and initial velocity of the system, the first dynamic load (the force $\dot{F}_0$) is applied linearly at the middle of the solid body in the y direction within a time range [0, 0.25] s and discharged linearly within

Details of "Pinned_Base"	
Scope	
Scoping Method	Geometry Selection
Geometry	1 Face
Coordinate System	Global Coordinate System
X Coordinate	0, mm
Y Coordinate	0, mm
Z Coordinate	0, mm
Location	Click to Change
Definition	
Type	Remote Displacement
X Component	0, mm (step applied)
Y Component	0, mm (step applied)
Z Component	0, mm (step applied)
Rotation X	0, ° (step applied)
Rotation Y	0, ° (step applied)
Rotation Z	Free
Suppressed	No
Behavior	Deformable

Details of "Pinned_Tip"	
Scope	
Scoping Method	Geometry Selection
Geometry	1 Face
Coordinate System	Global Coordinate System
X Coordinate	50, mm
Y Coordinate	0, mm
Z Coordinate	0, mm
Location	Click to Change
Definition	
Type	Remote Displacement
X Component	Free
Y Component	0, mm (step applied)
Z Component	0, mm (step applied)
Rotation X	0, ° (step applied)
Rotation Y	0, ° (step applied)
Rotation Z	Free
Suppressed	No
Behavior	Deformable

Figure 6.18: Boundary conditions–base and tip of the Model 2

a time range [0.25, 0.5] s. The maximum values of the force is $F_0 = 10^{-7}$ N. These are the load steps 1 and 2, during which the initial deflection of the beam occurs. The third main load step is within a time range [0.25, 30] s. The periodic excitation load $P(t)$ is applied during load steps 2 and 3. The sequence of the three load steps of the model is similar to the Model 1 and presented in the Fig. 6.9. The configuration of loads and boundary conditions of the Model 2 in the instant 0.3505 s is shown in the Fig. 6.19.

In the analysis settings, the minimum time step is defined 1e-3 s, and the maximum time step is defined 1e-2 s (Fig. 6.10).

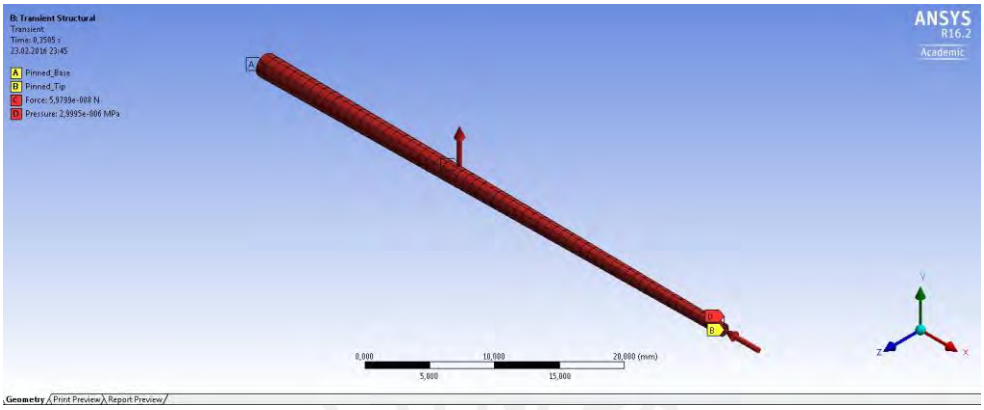

Figure 6.19: Model 2 of the parametrically excited TCB

Simulation results

In this case, the aim of the simulations is to find numerically the region of the principal parametric resonance of the TCB. That is why the numerical simulations of the transient analysis are made for the excitation frequencies close to the doubled first natural vibration frequency of the beam: $\Omega \approx 2\omega_0$.

The results of simulations show that the Model 2 of the TCB exhibits parametrical resonance vibrations within the following *region of the principal parametric resonance*:

$$\text{Simulation:} \quad 1.32 \text{ ™ } \nu \text{ ™ } 1.50 \text{ Hz} \tag{6.4}$$

According to chapter 4.7, for the chosen values of the simulation parameters the first natural vibration frequency of the TCB is $\omega_0 = 0.7869$ Hz and the dimensionless parameter $\varepsilon = 0.2124$, see (4.52). As it was shown before, the theoretical region of the principal parametric resonance depends on ε and ω_0 and it is within a range (4.52):

$$\text{Theory:} \quad 1.48 < \nu < 1.65 \text{ Hz}.$$

Thus, it may be concluded that the accounting of the variable cross-section of the beam leads to a slight discrepancy between the theoretical and numerical results.

For example, for the excitation frequency $\nu = 1.4180$ Hz, which is within the numerical region of the principal parametric resonance (6.4), the transverse displacement of the cross-section of the SCB at $x = L/2$ is presented

in Fig. 6.20. It is obvious that the parametric resonance takes place, and the amplitude of the vibrations increases exponentially with time. Moreover, the averaged amplitude $a_0(t)$ of parametric vibrations, calculated according to the theoretical analysis in chapter 4.7, is plotted for the initial amplitude value $a_0(0)$ = 0.18 mm. Note that the theoretical averaged amplitude $a_0(t)$ of the TCB differs in time from the amplitude of the numerical result, since the nonlinear behaviour of the system due to the large deflections occurs.

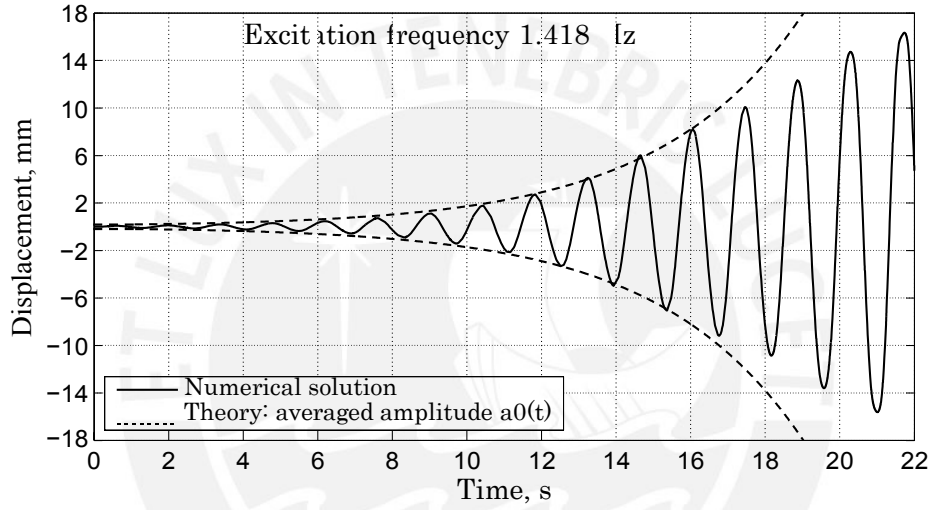

Figure 6.20: Transverse displacement of the cross-section of the SCB at $x = L/2$ for the excitation frequency ν = 1.48 Hz, ω_0 = 0.7869 Hz and ε = 0.2124. Solid line – the result of the numerical simulations; dashed line – the averaged amplitude $a_0(t)$ obtained theoretically for $a_0(0)$ = 0.18 mm

Figure 6.21 shows the steady state response of the system to the frequency ν = 1.30 Hz, which is outside the numerical region of the principal parametric resonance of the TCB (6.4). It shows the transverse displacement of the cross-section of the TCB at $x = L/2$. Moreover, the averaged amplitude $a_0(t)$ of parametric vibrations, calculated according to the theoretical analysis in chapter 4.7, is plotted for the excitation frequency ν = 1.461 Hz, the initial amplitude value $a_0(0)$ = 0.078 mm and $\theta(0)$ = 1.7453.

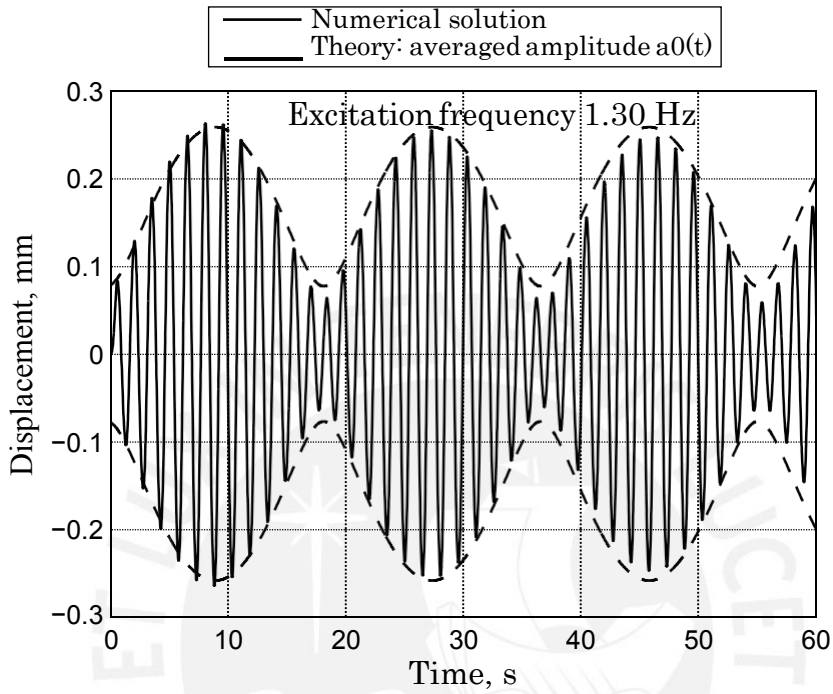

Figure 6.21: Transverse displacement of the cross-section of the TCB at $x = L/2$ for the excitation frequency $\nu = 1.30$ Hz, $\omega_0 = 0.7869$ Hz and $\varepsilon = 0.2124$. Solid line – the result of the numerical simulations; dashed line – the averaged amplitude $a_0(t)$ obtained theoretically for $\nu = 1.461$ Hz, $a_0(0) = 0.078$ mm and $\theta(0) = 1.7453$

6.4 Simulation for Model 3 – Circular cylindrical beam (CCB)

6.4.1 Geometry and properties of the model

An CCB (Model 3) is modeled in ANSYS 16.2 Workbench as a circular cylindrical line element. The model has the constant circular cross-section with a radius r_b, the length L and the constant curvature radius R_0. The material parameters, the density ρ and the Young's modulus E, are same as for Models 1 and 2. The values of the parameters are given in table 5.

According to the theoretical model in the chapter 5, the periodic force perpendicular to the cross-section at the tip of the beam is applied (Fig. 5.1). Since it is not possible to apply a following force to the cross-section of the line body, it is necessary to define a solid body — a circular cylinder, which is attached to the line body. The parameters of the cylinder are listed in table 5. The cylinder can be considered massless, since the mass of it is defined to be small (close to zero). Figure 6.22 shows the geometry of the model.

Table 5: Properties of the model 3 of the CCB

MODEL 3		
	Line Body	Solid body
L (mm)	51.323	1
r_b (mm)	1	1
ρ (kg/m^3)	1000	1e-6
E (N/m^2)	10313	2e+13
R_0 (mm)	65	

In the present numerical simulation for the Model 3, the beam element (beam188) is used for the line body, and the solid element (solid186) is used for the cylinder (Fig. 6.22, right). The number of elements of the line body is 52 and of the solid cylinder is 16. The total number of nodes is 198.

The transition between elements of the line and solid bodies is defined with the bonded type of contact MPC, similar to the Model 1 see Fig. 6.5.

The corresponding pinned–pinned boundary conditions for the model are applied as following. The left end point of the line body is pinned. It means that there is no displacement in all three directions and the rotation only

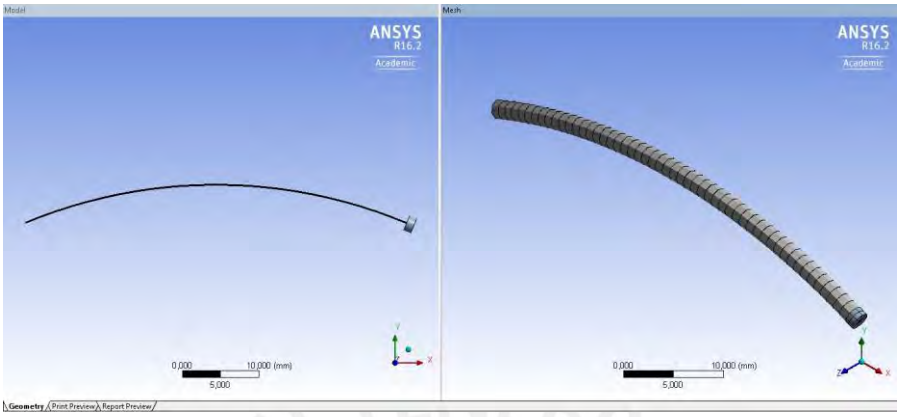

Figure 6.22: (a) Geometry of the Model 3; (b) Meshing of the Model 3 with beam and solid elements

around the z axis is free. The left cross-section of the solid body (cylinder) is pinned with free displacement along the x axis and free rotation around the z axis. In the model, the damping is not consider. The numerical damping is defined manually to be equal zero.

6.4.2 Modal analysis of the natural vibration frequencies

This chapter contains numerical results of the natural vibration frequencies of the CCB for the parameters listed in table 5.

The numerical results of the first three transverse natural frequencies of the CCB are given in the table 6. The mode shapes of the CCB obtained numerically for the beam188 elements in ANSYS 16.2 Workbench are shown in Fig. 6.23.

Table 6: Numerical natural vibration frequencies of the CCB in Hz

Modal Analysis	
	Numerical results
ω_1	0.9302
ω_2	3.6778
ω_3	8.4661

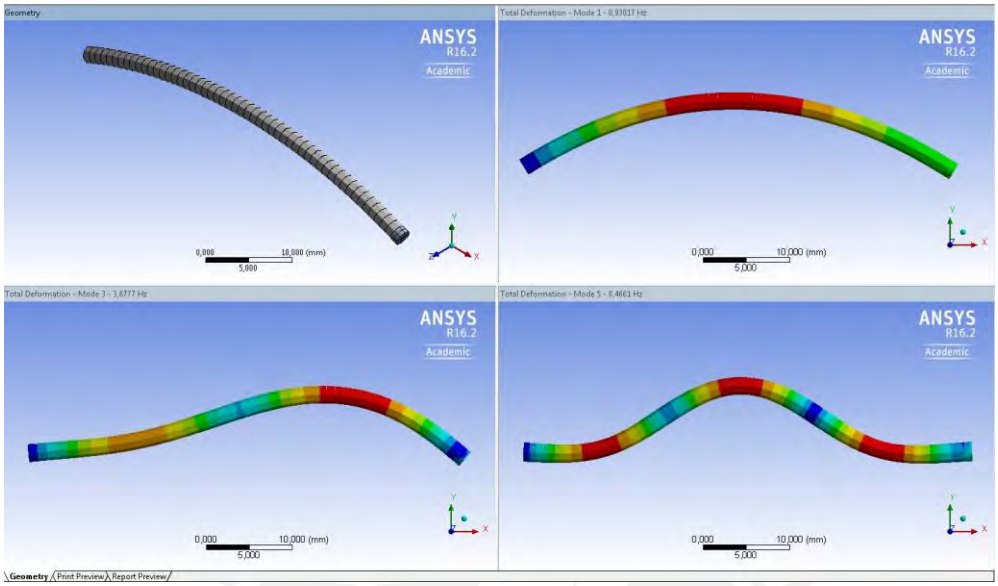

Figure 6.23: Mode shapes of transverse vibrations of the CCB

6.4.3 Transient analysis of the parametric excited CCB

The response of the CCB on the parametric excitation is simulated in the analysis system "Transient structural", ANSYS 16.2 Workbench, in the same manner as for the Models 1 in section 6.2.3. The system is meshed by beam188 and solid186 elements to evaluate the transient analysis. The boundary conditions is shown in Fig. 6.24.

The time-varying load is defined as a periodic following pressure $P(t) = -P_0 \cos(\Omega t)$ normal to the cross-section of the solid body. The amplitude of the pressure is P_0 = 3 Pa. Thus, the periodic force acting on the system is $\dot{F}(t) = \pi r_t^2 P(t) \dot{n}_t$, where $\dot{n}_t$ is the normal vector to the cross-section. Note that the replacement of the normal force with pressure is necessary to ensure a load in direction of the normal cross-section of the deformed beam.

The applying load process in the model is developed in three steps. To create an initial displacement and initial velocity of the system, the first dynamic load (the force $\dot{F}_0$) is applied linearly at the middle of the line body in the y direction within a time range $[0, 0.25]$ s and discharged linearly within a time range [0.25, 0.5] s. The maximum values of the force is $F_0 = 10^{-7}$ N. These are the load steps 1 and 2, during which the initial deflection of the beam occurs. The third main load step is within a time range [0.25, 30] s.

Details of "Pinned_base"

Scope	
Scoping Method	Geometry Selection
Geometry	1 Vertex
Coordinate System	Global Coordinate System
X Coordinate	0, mm
Y Coordinate	0, mm
Z Coordinate	0, mm
Location	Click to Change
Definition	
Type	Remote Displacement
X Component	0, mm (step applied)
Y Component	0, mm (step applied)
Z Component	0, mm (step applied)
Rotation X	0, ° (step applied)
Rotation Y	0, ° (step applied)
Rotation Z	Free
Suppressed	No

Details of "Pinned_Tip"

Scope	
Scoping Method	Geometry Selection
Geometry	1 Face
Coordinate System	Global Coordinate System
X Coordinate	50, mm
Y Coordinate	0, mm
Z Coordinate	0, mm
Location	Click to Change
Definition	
Type	Remote Displacement
X Component	Free
Y Component	0, mm (step applied)
Z Component	0, mm (step applied)
Rotation X	0, ° (step applied)
Rotation Y	0, ° (step applied)
Rotation Z	Free
Suppressed	No

Figure 6.24: Boundary conditions at the base and at the tip of the model

The periodic excitation load $P(t)$ is applied during load steps 2 and 3. The sequence of the three load steps of the model is similar to the Model 1 and presented in the Fig. 6.9. The configuration of loads and boundary conditions of the Model 3 in the instant 0.25 s is shown in the Fig. 6.25.

In the analysis settings, the minimum time step is defined 1e-3 s, and the maximum time step is defined 1e-2 s (Fig. 6.10).

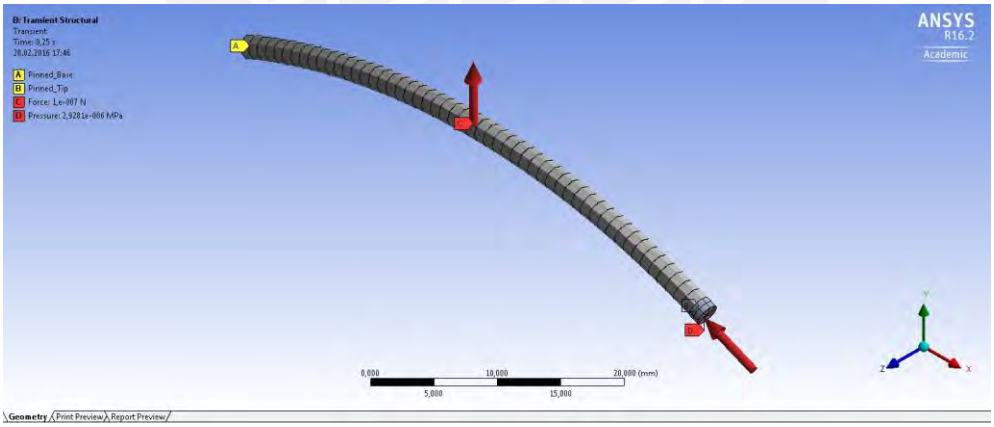

Figure 6.25: Model 3 of the parametrically excited CCB

Simulation results

The aim of the simulations is to find numerically the region of the principal parametric resonance of the CCB. That is why the numerical simulations of the transient analysis are made for the excitation frequencies close to the doubled first natural vibration frequency of the beam: $\Omega \approx 2\omega_0$.

Figure 6.26 shows the response of the parametrical excitation frequency v = 1.86 Hz, which is near the range $\Omega \approx 2\omega_0$. Antisymmetric vibrations are obtained. It may be seen that the amplitude of the vibrations increases with the time until certain steady state value (approximately 1.7 mm), and then it is stabilized.

Figures 6.27 and 6.28 show the transverse displacement of the cross-section of the CCB at $x = L/2$ for two frequency values v = 1.96 Hz and v = 1.74 Hz, respectively. It may be seen that in these cases the response of the system is more complex. Within the time range [0, 30] s antisymmetric vibrations are observed.

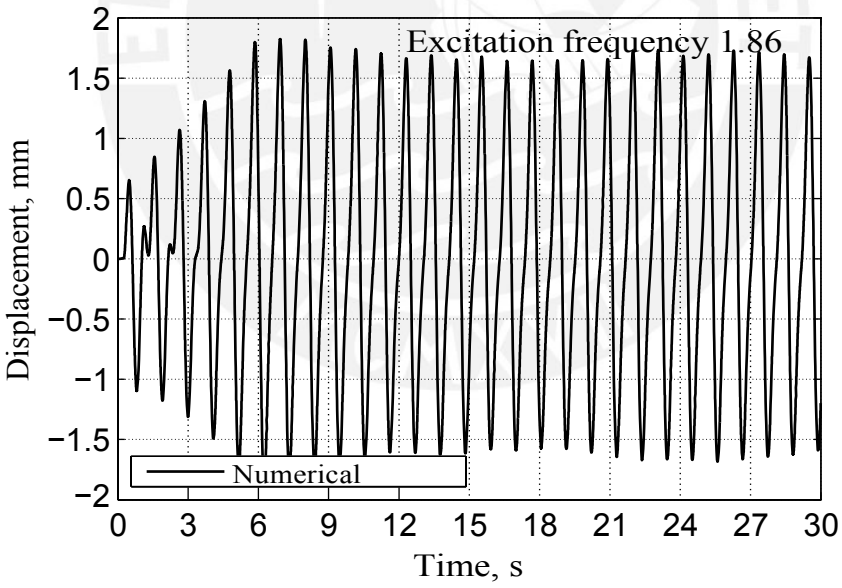

Figure 6.26: Transverse displacement of the cross-section of the CCB at $x = L/2$ for the excitation frequency v = 1.86 Hz and ω_0 = 0.9302 Hz

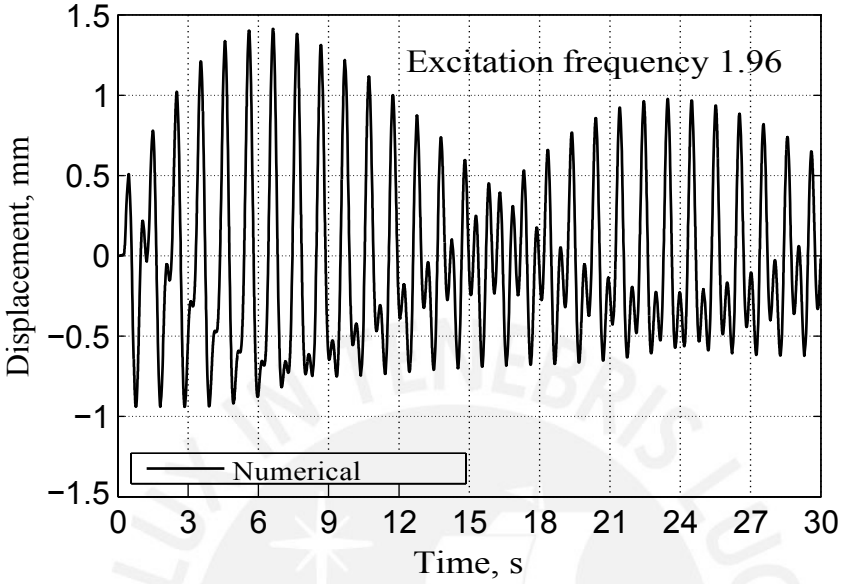

Figure 6.27: Transverse displacement of the cross-section of the CCB at $x = L/2$ for the excitation frequency v = 1.96 Hz and ω_0 = 0.9302 Hz

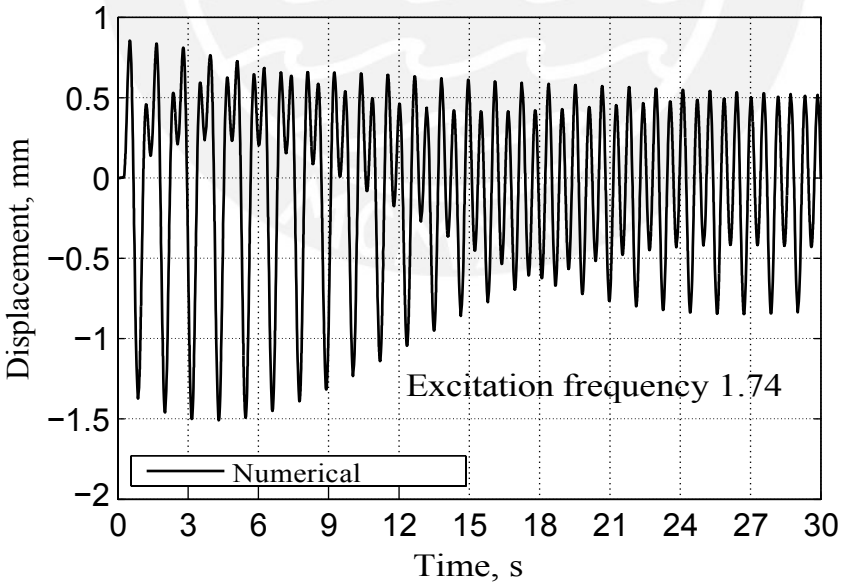

Figure 6.28: Transverse displacement of the cross-section of the CCB at $x = L/2$ for the excitation frequency v = 1.74 Hz and ω_0 = 0.9302 Hz

7 Conclusions and outlook

In nature, vibrissae are tactile hairs of mammals used as sensor elements for the exploring the surrounding area. These hairs, also known as whiskers, can be found in different locations on an animals body. Mystacial vibrissae are distributed over a whiskerpad on a muzzle and well organized in rows and columns. Carpal vibrissae are located on the downside aspect of the forelimbs of mammals. The vibrissal hair has a conical shape and grows from a special heavily innervated hair follicle incorporating a capsule of blood, called follicle-sinus complex. As the hair itself has no receptors along its length, the vibrissa may be considered as a system for transmitting forces and torques that arise from the contact between the hair and an object to sensory receptors inside the follicle.

In the present thesis, the vibrational motion of vibrissae during natural exploratory behaviour is analysed from the mechanical point of view. The phenomenon of the parametric resonance of the vibrissa is investigated theoretically and numerically. In the first part of this thesis, the following mechanical models of an elastic beam under an parametric excitation are studied theoretically based on findings in the literature:

1. An elastic beam with the straight neutral axis and circular cross-section (chapter 4):
    - Model 1: straight cylindrical beam (SCB) with the constant radius of the cross-section;
    - Model 2: truncated conical beam (TCB) with the linearly decreasing radius of the cross-section;
2. A curved elastic beam with the circular natural configuration and circular cross-section (chapter 5):
    - Model 3: circular cylindrical beam (CCB) with the constant radius of the cross-section.

Within these theoretical models, a periodic following force is applied perpendicular to the cross-section of the beam at the tip. The force corresponds to frictional interactions between the tip of the beam/vibrissa and a complex roughness profile of an investigated object.

Based on this simplified formulation of the problem, small transverse oscillations of the beam are analysed using the Euler-Bernoulli beam theory. The approximation of the equation of motion of the beam is obtained by means of asymptotic methods of mechanics: Galerkin's method and the method of averaging.

In the second part of the thesis (chapter 6), the numerical analysis of the problems is performed based on the finite element method using ANSYS 16.2 software. For each model, the dynamical mechanical response of the system on the parametric excitation is simulated for different frequency values. The numerical simulations of the natural vibration frequencies are made.

It is shown theoretically and numerically that at specific ranges of the excitation frequency the phenomenon of the parametric resonance of the beam takes place. That means that the amplitude of vibrations of the beam increases exponentially with time, when it is stimulated within one of the frequency ranges of the parametric resonance. These ranges depend on the geometrical and material parameters of the beam model, as well as the amplitude of the periodic excitation. The most response of the system on the parametrical excitation occurs close to the doubled first natural frequency of the system.

For the Model 1 (SCB), two ranges of the parametric resonance are obtained numerically: the region of the principal parametric resonance close to the doubled first natural frequency of the system and the second range, which is around the value of the first natural frequency. It is shown that the theoretical and numerical results correspond well to each other. Moreover, it is demonstrated that the response of the system on the parametrical excitation is qualitatively stronger within the range of the principal parametrical resonance than within the second range.

For the special case of the Model 2 (TCB), when the radius at the tip is two times smaller that the radius at the base, the difference between the theoretical and numerical values of the first vibration frequency is observed. It corresponds to the fact that the Rayleighs method gives the upper boundary for the theoretical value. Hence, there is a slight discrepancy in the ranges of the principal parametric resonance obtained theoretically and numerically. It is associated with the accounting of the variable radius of the cross-section.

For the Model 3 (CCB), the numerical results show that the response of the system on the parametric excitation with the frequency close to the doubled first natural vibration frequency is more complex. It may be seen that the amplitude of the vibrations increases with the time until certain

steady state value, and then it is stabilized.

Thus, it is shown theoretically and numerically that from the mechanical point of view the phenomenon of parametric resonance of the vibrissa is possible. It can lead to the fact that arbitrarily small deviations of a system would produce a large response, and the amplitude of vibrations would increase progressively (exponentially) in time. The phenomenon of parametric resonance may be used to distinguish and amplify specific periodic components of a complex roughness profile during vibrissal texture discrimination.

In future work, the present beam models of the vibrissa may be improved by considering simultaneously both the variable radius of the cross-section and variable natural configuration (intrinsic curvature) of the beam. Numerical simulations should be also performed using realistic values of the vibrissa parameters reported in the literature.

References

[1] C. Behn: Mathematical modeling and control of biologically inspired uncertain motion systems with Adaptive Features. Habilitation thesis. Technische Universität Ilmenau, Germany (2013)

[2] M. Schmidt, H. Witte, K. Zimmermann, S. Niederschuh, T. Helbig, D. Voges, I. Husung, T. Volkova, Ch. Will, C. Behn, J. Steigenberger, G. Klauer: Technical, non-visual characteritation of substrate contact using carpal vibrissae as a biological model. In: Proc. of the 58th International Scientific Colloquium, IWK 2014, Ilmenau, Germany, September 8-12, 2014.

[3] M.A. Neimark, M.L. Andermann, J.J. Hopfield, C.I. Moore: Vibrissa resonance as a transduction mechanism for tactile encoding. The Journal of Neuroscience 23 (2003) 6499-6509.

[4] D. Voges, K. Carl, G.J. Klauer, R. Uhlig, C. Schilling, C. Behn, H. Witte: Structural characterization of the whisker system of the rat. IEEE Sensors Journal 12 (2) (2012) 332-339.

[5] J. Dörfl: The musculature of the mystacial vibrissae of the white mouse. Journal of Anatomy 135 (1982) 147-154.

[6] S. Haidarliu, E. Simony, D. Golomb, E. Ahissar: Muscle architecture in the mystacial pad of the rat. The Anatomical Record 293 (2010) 1192-1206.

[7] R. Towal, B. Quist, V. Gopal, J. Solomon, M. Hartmann: The morphology of the rat vibrissal array: a model for quantifying spatiotemporal patterns of whisker-object contact. PLoS Comput. Biol. 7 (2011) e1001120.

[8] B. Quist, M. Hartmann: Mechanical signals at the base of a rat vibrissa: the effect of intrinsic vibrissa curvature and implications for tactile exploration. Journal of Neurophysiology 107 (2012) 2298–2312.

[9] G.E. Carvell, D.J. Simons: Biometric analyses of vibrissal tactile discrimination in the rat, The Journal of Neuroscience 10 (1990) 2638-2648.

[10] G. Dehnhardt, A. Kaminski: Sensitivity of the mystacial vibrissae of harbour seals (phoca vitulina) for size differences of actively touched objects. J. Exp. Biol. 198 (1995) 2317-2323.

[11] M.L. Andermann, C.I. Moore: Mechanical resonance enhances the sensitivity of the vibrissa sensory system to near-threshold stimuli. Brain Research 1235 (2008) 74-81.

[12] M.J. Hartmann, N.J. Johnson, R.B. Towal, C. Assad: Mechanical characteristics of rat vibrrissae: Resonant frequencies and damping in isolated whiskers and in the awake behaving animal. The Journal of Neuroscience 23 (2003) 6510-6519.

[13] E. Arabzadeh, E. Zorzin, M. Diamond: Neuronal encoding of texture in the whisker sensory pathway. PLoS Biol. 3 (2005) e17.

[14] J. Hipp, E. Arabzadeh, E. Zorzin, J. Conradt, C. Kayser, M. Diamond, P. Konig: Texture signals in whisker vibrations. Journal of Neurophysiology 95 (2006) 1792-1799.

[15] M. von Heimendahl, P. Itskov, E. Arabzadeh, M. Diamond: Neuronal activity in rat barrel cortex underlying texture discrimination. PLoS Biol. 5 (2007) e305.

[16] J. Wolfe, D. Hill, S. Pahlavan, P. Drew, D. Kleinfeld, D. Feldman: Texture coding in the rat whisker system: slip-stick versus differential resonance. PLoS Biol. 6 (2008) e215.

[17] E. Lottem, R. Azouz, Mechanisms of tactile information transmission through whisker vibrations. J. Neurosci. 29 (2009) 11686-11697.

[18] L. Garion, U. Dubin, Y. Rubin, M. Khateb, Y. Schiller, R. Azouz, J. Schiller: Texture coarseness responsive neurons and their mapping in layer 23 of the rat barrel cortex in vivo. eLife 3 (2014) e03405.

[19] R. Berg, D. Kleinfeld: Rhythmic whisking by rat: retraction as well as protraction of the vibrissae is under active muscular control. Journal of Neurophysiology 89 (2003) 104-117.

[20] C. Behn, T. Schmitz, H. Witte, K. Zimmermann: Animal vibrissae: modelling and adaptive control of bio-inspired sensors. In: Proc. of the 12th International Work-Conference on Artificial Neural Networks, IWANN 2013, Tenerife, Spain, June 12-14, 2013, pp. 159-170.

[21] T. Schmitz, C. Behn: Analytical investigations and adaptive control of vibrissae-like sensor models with finite dof. In: Proc. of the 56th International Scientific Colloquium, IWK 2011, Ilmenau, Germany, September 12-16, 2011.

[22] G. Scholz, C. Rahn: Profile sensing with an actuated whisker. IEEE Transactions on Robotics and Automation 20 (2004) 124-127.

[23] M. Schäfer, T. Schmitz, C. Will, C. Behn: Transversal vibrations of beams with boundary damping in the context of animal vibrissae. In: Proc. of the 56th International Scientific Colloquium, IWK 2011, Ilmenau, Germany, September 12-16, 2011.

[24] J. Steigenberger: A continuum model of passive vibris- sae. Preprint No. M 13/03, Technische Universität Ilmenau, Fakultät für Mathematik, Ilmenau, Germany (2013).

[25] C. Will, J. Steigenberger, C. Behn: Object contour reconstruction using bio-inspired sensors. In: Proc. of the 11th International Conference on Informatics in Control, Automation and Robotics, ICINCO 2014, Vienna, Austria, September 01-03, 2014, pp. 459-467.

[26] U. Zimmer: Self-localization in dynamic environments. In: IEEE/SOFT International Workshop BIES'95, Tokio, Japan, May 30-31, 1995, p. 8.

[27] M. Fend, S. Bovet, V. Hafner: The artifficial mouse-a robot with whiskers and vision. In: 35th International Symposium on Robotics, ISR 2004, Paris, 610 France, March 23-26, 2004.

[28] M. Fend, H. Yokoi, R. Pfeifer: Optimal morphology of a biologicallyinspired whisker array on an obstacle-avoiding robot. In:

Advances in Artifficial Life, Proc. of 7th European Conference, ECAL 2003, Dortmund, Germany, September 14-17, 2003, Vol. 2801 of LNAI, Springer, Eds. J.G. Carbonell and J. Siekmann, 2003.

[29] M. Pearson, A. Pipe, C. Melhuish, B. Mitchinson, T. Prescott: Whiskerbot: A robotic active touch system modeled on the rat whisker sensory system. Adapt. Behav. 15 (2007) 223-240.

[30] M. Pearson, B. Mitchinson, J. Sullivan, A. Pipe, T. Prescott: Biomimetic vibrissal sensing for robots. Phil. Trans. R. Soc. B 366 (2011) 3085-3096.

[31] Y. Zuo, I. Perkon, M. Diamond: Whisking and whisker kinematics during a texture classification task. Philosophical Transactions of the Royal Society B 366 (2011) 30583069.

[32] T. Volkova, I. Zeidis, H. Witte, M. Schmidt, K. Zimmermann: Analysis of the vibrissa parametric resonance causing a signal amplification during whisking behaviour. Preprint submitted to Journal of Bionic Engineering (2015).

[33] http://www.wsdot.wa.gov/TNBhistory/Connections /connections3.htm

[34] M. Cartmell: Introduction to Linear, Parametric and Nonlinear Vibrations. Chapman and Hall (1990).

[35] A. Nayfeh and D. Mook: Nonlinear Oscillations. John Wiley and Sons, New York, Inc (1995).

[36] G. Hill: On the Part of the Motion of Lunar Perigee which is a Function of the Mean Motions of the Sun and Moon. Acta Math. 8 (1) (1886) 136.

[37] N. McLachlan: Theory and application of Mathieu functions. Dover Publications (1964).

[38] E. Mathieu: Mémoire sur Le Mouvement Vibratoire dune Membrane de forme Elliptique. Journal de Mathématiques Pures et Appliquées 13 (1868) 137-203.

[39] E. Witmer: Elementary Bernoulli-Euler Beam theory. MIT Unified Engineering Course Notes (1991-1992) pp. 5114 to 5164.

[40] W.T. Thomson: Theory of vibration with applications. Prentice-Hall (1981).

[41] S. Timoshenko: Theory of structures. McGraw-Hill, Inc (1965).

[42] G. Temple and W. Bickley: Rayleigh's Principle and Its Application to Engineering. Dover, New York (1956).

[43] S. Timoshenko: On the correction factor for shear of the differential equation for transverse vibrations of bars of uniform cross-section. Philosophical Magazine (1921) p. 744.

[44] S. Rao: Mechanical vibrations. Prentice Hall (2010).

[45] V. Bolotin: The dynamic stability of elastic systems. Holden-Day, Inc (1964).

[46] V. Svetlitsky: Dynamics of Rods. Springer (2004).

[47] L. Kantorovich, V.Krylov: Approximate methods of higher analysis. Interscience Publ., New York (1958).

[48] N. Bogolyubov, Y. Mitropoliskii: Asymptotic methods in the theory of non-linear oscillations. Gordon and Breach Science Publishers, New York (1961).

[49] L. Landau and E. Lifshitz: Mechanics, 2nd Edition, Vol.1 of Course of theoretical physics. Pergamon Press, Oxford (1969).

[50] I.Malkin: Theory of stability of motion. United States Atomic Energy Commission, Washington (1959).

[51] ANSYS online Help. ANSYS Release 15.0 SAS IP, INC. (2013).

Appendix A: Report ”Transient Analysis” for the Model 1 (ANSYS 16.2 Workbench)

Project

First Saved	Monday, November 16, 2015
Last Saved	Monday, December 07, 2015
Product Version	16.2 Release
Save Project Before Solution	No
Save Project After Solution	No

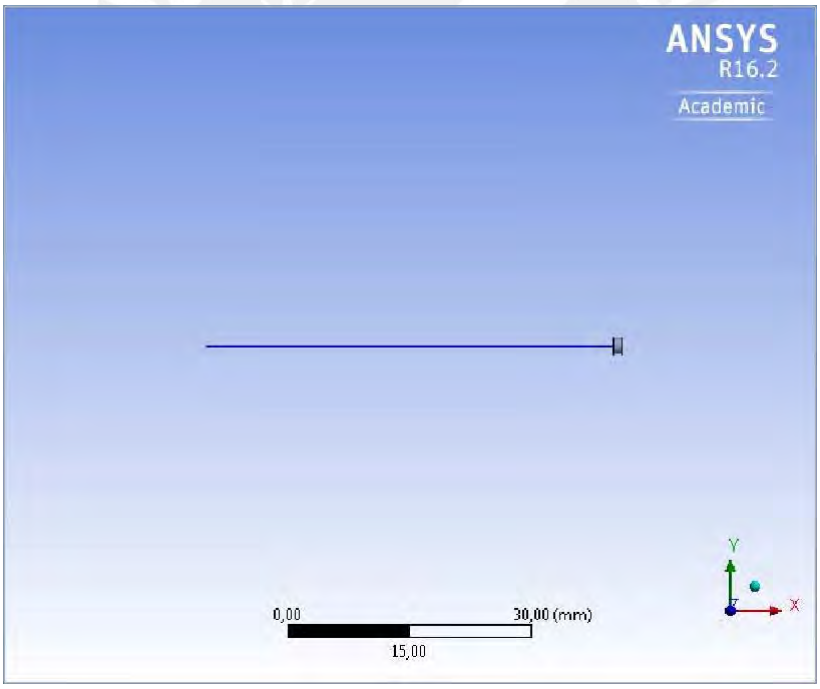

1

Contents

Report Not Finalized

Not all objects described below are in a finalized state. As a result, data may be incomplete, obsolete or in error. View first state problem. To finalize this report, edit objects as needed and solve the analyses.

Units

TABLE 1

Unit System	Metric (mm, kg, N, s, mV, mA) Degrees rad/s Celsius
Angle	Degrees
Rotational Velocity	rad/s
Temperature	Celsius

Model (B4)

Geometry

TABLE 2
Model (B4) > Geometry

Object Name	*Geometry*
State	Fully Defined
Definition	
Source	D:\Benutzerdaten\StudentCesar\ANSYS_Model1_CSB\Principle_Range\Model1_CSB_Freq2.01\Model1_CSB_files\dp0\Geom\DM\Geom.agdb
Type	DesignModeler
Length Unit	Meters
Element Control	Program Controlled
Display Style	Body Color
Bounding Box	
Length X	51, mm
Length Y	2, mm
Length Z	2, mm
Properties	
Volume	160,21 mm³
Mass	1,5707e-004 kg
Scale Factor Value	1,
Statistics	
Bodies	2
Active Bodies	2
Nodes	194
Elements	66
Mesh Metric	Element Quality
Min	0,839097059212787
Max	0,839111304391343
Average	0,839104181802065
Standard Deviation	7,35614855417366E-06
Basic Geometry Options	

Parameters	Yes
Parameter Key	DS
Attributes	No
Named Selections	No
Material Properties	No
Advanced Geometry Options	
Use Associativity	Yes
Coordinate Systems	No
Reader Mode Saves Updated File	No
Use Instances	Yes
Smart CAD Update	No
Compare Parts On Update	No
Attach File Via Temp File	Yes
Temporary Directory	C:\Users\StudentCesar\AppData\Roaming\Ansys\v150
Analysis Type	3-D
Decompose Disjoint Geometry	Yes
Enclosure and Symmetry Processing	Yes

TABLE 3
Model (B4) > Geometry > Parts

Object Name	*Line Body*	*Solid*
State	Meshed	
Graphics Properties		
Visible	Yes	
Transparency	1	
Definition		
Suppressed	No	
Coordinate System	Default Coordinate System	
Reference Temperature	By Environment	
Offset Mode	Refresh on Update	
Offset Type	Centroid	
Model Type	Beam	
Stiffness Behavior		Flexible
Material		
Assignment	Material_Beam	Material_Null
Nonlinear Effects	Yes	
Thermal Strain Effects	Yes	
Bounding Box		
Length X	50, mm	1, mm
Length Y	0, mm	2, mm
Length Z	0, mm	2, mm
Properties		
Volume	157,07 mm³	3,1416 mm³
Mass	1,5707e-004 kg	3,1416e-015 kg
Length	50, mm	
Cross Section	Circular1	
Cross Section Area	3,1414 mm²	
Cross Section IYY	0,78529 mm²·mm²	
Cross Section IZZ	0,78529 mm²·mm²	
Centroid X		50,5 mm
Centroid Y		-2,9613e-016 mm
Centroid Z		2,6769e-016 mm
Moment of Inertia Ip1		1,5549e-015 kg·mm²
Moment of Inertia Ip2		1,0379e-015 kg·mm²
Moment of Inertia Ip3		1,0379e-015 kg·mm²
Statistics		
Nodes	101	93
Elements	50	16
Mesh Metric	Element Quality	
Min	0	0,839097059212787
Max	0	0,839111304391343
Average	0	0,839104181802065
Standard Deviation	0	7,35614855417366E-06

Coordinate Systems

TABLE 4
Model (B4) > Coordinate Systems > Coordinate System

Object Name	*Global Coordinate System*
State	Fully Defined
Definition	
Type	Cartesian
Coordinate System ID	0,
Origin	

Origin X	0, mm
Origin Y	0, mm
Origin Z	0, mm
Directional Vectors	
X Axis Data	[1, 0, 0,]
Y Axis Data	[0, 1, 0,]
Z Axis Data	[0, 0, 1,]

Connections

TABLE 5
Model (B4) > Connections

Object Name	*Connections*
State	Fully Defined
Auto Detection	
Generate Automatic Connection On Refresh	Yes
Transparency	
Enabled	Yes

TABLE 6
Model (B4) > Connections > Contacts

Object Name	*Contacts*
State	Fully Defined
Definition	
Connection Type	Contact
Scope	
Scoping Method	Geometry Selection
Geometry	All Bodies
Auto Detection	
Tolerance Type	Slider
Tolerance Slider	0,
Tolerance Value	0,1277 mm
Use Range	No
Face/Face	No
Face/Edge	No
Edge/Edge	No
Priority	Include All
Group By	Bodies
Search Across	Bodies
Statistics	
Connections	1
Active Connections	1

TABLE 7
Model (B4) > Connections > Contacts > Contact Regions

Object Name	*Bonded - Line Body To Solid*
State	Fully Defined
Scope	
Scoping Method	Geometry Selection
Contact	1 Vertex
Target	1 Face
Contact Bodies	Line Body
Target Bodies	Solid
Definition	
Type	Bonded
Scope Mode	Manual
Behavior	Program Controlled
Trim Contact	Program Controlled
Suppressed	No
Advanced	
Formulation	MPC
Constraint Type	Target Normal, Couple U to ROT
Pinball Region	Radius
Pinball Radius	0,25 mm
Geometric Modification	
Target Geometry Correction	None

Mesh

TABLE 8
Model (B4) > Mesh

Object Name	*Mesh*
State	Solved
Display	
Display Style	Body Color
Defaults	
Physics Preference	Mechanical

Relevance	0
Sizing	
Use Advanced Size Function	Off
Relevance Center	Coarse
Element Size	Default
Initial Size Seed	Active Assembly
Smoothing	Medium
Transition	Fast
Span Angle Center	Coarse
Minimum Edge Length	6,28320 mm
Inflation	
Use Automatic Inflation	None
Inflation Option	Smooth Transition
Transition Ratio	0,272
Maximum Layers	5
Growth Rate	1,2
Inflation Algorithm	Pre
View Advanced Options	No
Patch Conforming Options	
Triangle Surface Mesher	Program Controlled
Patch Independent Options	
Topology Checking	Yes
Advanced	
Number of CPUs for Parallel Part Meshing	Program Controlled
Shape Checking	Standard Mechanical
Element Midside Nodes	Program Controlled
Straight Sided Elements	No
Number of Retries	Default (4)
Extra Retries For Assembly	Yes
Rigid Body Behavior	Dimensionally Reduced
Mesh Morphing	Disabled
Defeaturing	
Pinch Tolerance	Please Define
Generate Pinch on Refresh	No
Automatic Mesh Based Defeaturing	On
Defeaturing Tolerance	Default
Statistics	
Nodes	194
Elements	66
Mesh Metric	Element Quality
Min	0,8391
Max	0,83911
Average	0,8391
Standard Deviation	7,3561e-006

TABLE 9
Model (B4) > Mesh > Mesh Controls

Object Name	*Edge Sizing*	*Body Sizing*	*Sweep Method*
State	Fully Defined		
Scope			
Scoping Method	Geometry Selection		
Geometry	1 Edge	1 Body	
Definition			
Suppressed	No		
Type	Element Size		Number of Divisions
Element Size	1, mm	0,8 mm	
Behavior	Soft		
Bias Type	No Bias		
Method			Sweep
Element Midside Nodes			Use Global Setting
Src/Trg Selection			Manual Source and Target
Source			1 Face
Target			1 Face
Free Face Mesh Type			All Tri
Sweep Num Divs			Default
Sweep Bias Type			No Bias
Element Option			Solid

Named Selections

TABLE 10
Model (B4) > Named Selections > Named Selections

Object Name	*Selection*
State	Fully Defined
Scope	
Scoping Method	Worksheet
Geometry	1 Node

Definition	
Send to Solver	Yes
Visible	Yes
Program Controlled Inflation	Exclude
Statistics	
Type	Manual
Total Selection	1 Node
Suppressed	0
Used by Mesh Worksheet	No
Tolerance	
Tolerance Type	Program Controlled
Zero Tolerance	1,e-008
Relative Tolerance	1,e-003

Transient (B5)

TABLE 11
Model (B4) > Analysis

Object Name	*Transient (B5)*
State	Not Solved
Definition	
Physics Type	Structural
Analysis Type	Transient
Solver Target	Mechanical APDL
Options	
Environment Temperature	22, °C
Generate Input Only	No

TABLE 12
Model (B4) > Transient (B5) > Initial Conditions

Object Name	*Initial Conditions*
State	Fully Defined

TABLE 13
Model (B4) > Transient (B5) > Initial Conditions > Initial Condition

Object Name	*Modal (None)*
State	Fully Defined
Definition	
Pre-Stress Environment	None

TABLE 14
Model (B4) > Transient (B5) > Analysis Settings

Object Name	*Analysis Settings*
State	Fully Defined
Restart Analysis	
Restart Type	Program Controlled
Load Step	3
Substep	5393
Time	11,494 s
Step Controls	
Number Of Steps	3,
Current Step Number	3,
Step End Time	30, s
Auto Time Stepping	On
Define By	Time
Carry Over Time Step	Off
Initial Time Step	1,e-002 s
Minimum Time Step	1,e-003 s
Maximum Time Step	1,e-002 s
Time Integration	On
Solver Controls	
Solver Type	Direct
Weak Springs	Program Controlled
Large Deflection	On
Restart Controls	
Generate Restart Points	Program Controlled
Retain Files After Full Solve	No
Nonlinear Controls	
Newton-Raphson Option	Program Controlled
Force Convergence	Program Controlled
Moment Convergence	Program Controlled
Displacement Convergence	Program Controlled
Rotation Convergence	Program Controlled
Line Search	Program Controlled
Stabilization	Off

Output Controls	
Stress	Yes
Strain	Yes
Nodal Forces	No
Contact Miscellaneous	No
General Miscellaneous	No
Store Results At	All Time Points
Damping Controls	
Stiffness Coefficient Define By	Direct Input
Stiffness Coefficient	0,
Mass Coefficient	0,
Numerical Damping	Manual
Numerical Damping Value	0
Analysis Data Management	
Solver Files Directory	D:\Benutzerdaten\StudentCesar\ANSYS_Model1_CSB\Principle_Range\Model1_CSB_Freq2.01\Model1_CSB_files\dp0\SYS-9\MECH\
Future Analysis	None
Scratch Solver Files Directory	
Save MAPDL db	No
Delete Unneeded Files	Yes
Nonlinear Solution	Yes
Solver Units	Active System
Solver Unit System	nmm

TABLE 15
Model (B4) > Transient (B5) > Analysis Settings
Step-Specific "Step Controls"

Step	Step End Time	Carry Over Time Step
1	0,25 s	
2	0,5 s	Off
3	30, s	Off

TABLE 16
Model (B4) > Transient (B5) > Analysis Settings
Step-Specific "Nonlinear Controls"

Step	Force Convergence	--Value	--Tolerance	--Minimum Reference
1	On	Calculated by solver	0,5%	2,415e-012 N
2	Program Controlled			
3				

TABLE 17
Model (B4) > Transient (B5) > Loads

Object Name	*festlager*	*loslager*	*Force*	*Pressure*
State	Fully Defined			
Scope				
Scoping Method	Geometry Selection			
Geometry	1 Vertex	1 Face	1 Edge	1 Face
Coordinate System	Global Coordinate System			
X Coordinate	0, mm	50, mm		
Y Coordinate	0, mm			
Z Coordinate	0, mm			
Location	Defined			
Definition				
Type	Remote Displacement		Force	Pressure
X Component	0, mm (step applied)	Free	Tabular Data	
Y Component	0, mm (step applied)		Tabular Data	
Z Component	0, mm (step applied)		Tabular Data	
Rotation X	0, ° (step applied)			
Rotation Y	0, ° (step applied)			
Rotation Z	Free			
Suppressed	No			
Rotation X		0, ° (step applied)		
Rotation Y		0, ° (step applied)		
Rotation Z		Free		
Behavior		Deformable		
Define By			Components	Normal To
Coordinate System			Global Coordinate System	
Magnitude				= -0,000003*cos(12,6493*time)
Advanced				
Pinball Region	All			
Function				
Unit System				Metric (mm, kg, N, s, mV, mA) Radians rad/s Celsius
Angular Measure				Radians
Graph Controls				
Number Of Segments				600,

FIGURE 1
Model (B4) > Transient (B5) > festlager

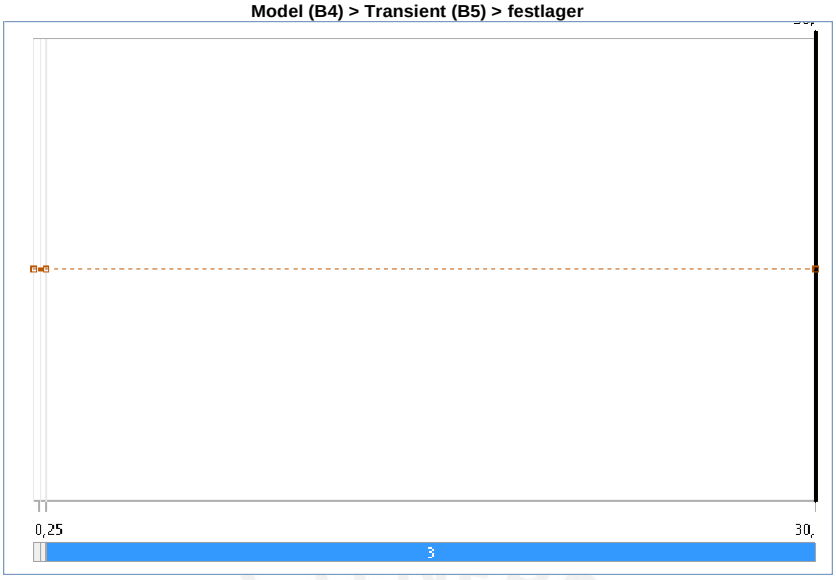

FIGURE 2
Model (B4) > Transient (B5) > loslager

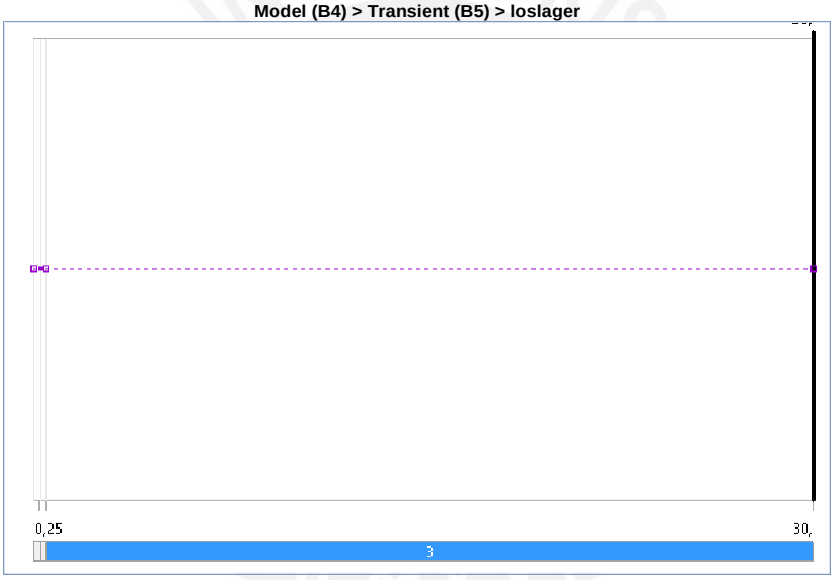

FIGURE 3
Model (B4) > Transient (B5) > Force

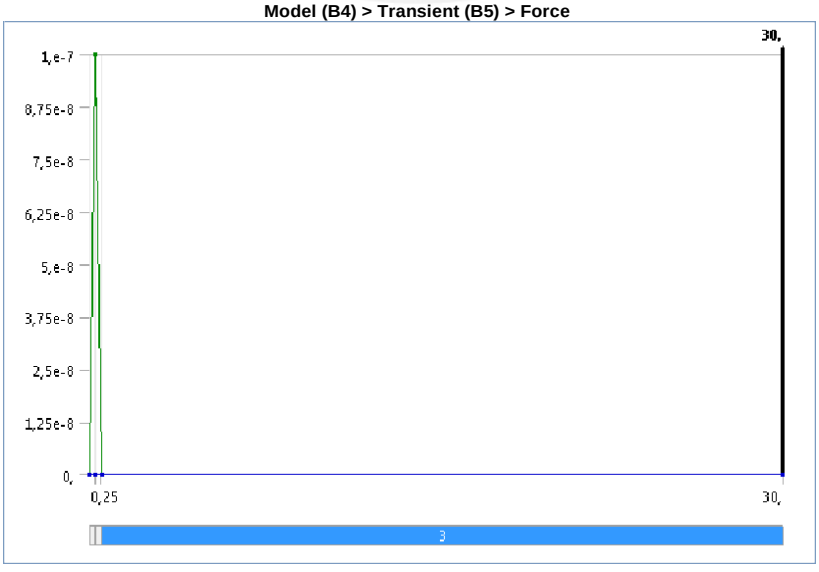

TABLE 18
Model (B4) > Transient (B5) > Force

Steps	Time [s]	X [N]	Y [N]	Z [N]
1	0,	0,	0,	0,
	0,25		1,e-007	
2	0,5		0,	
3	30,			

FIGURE 4
Model (B4) > Transient (B5) > Pressure

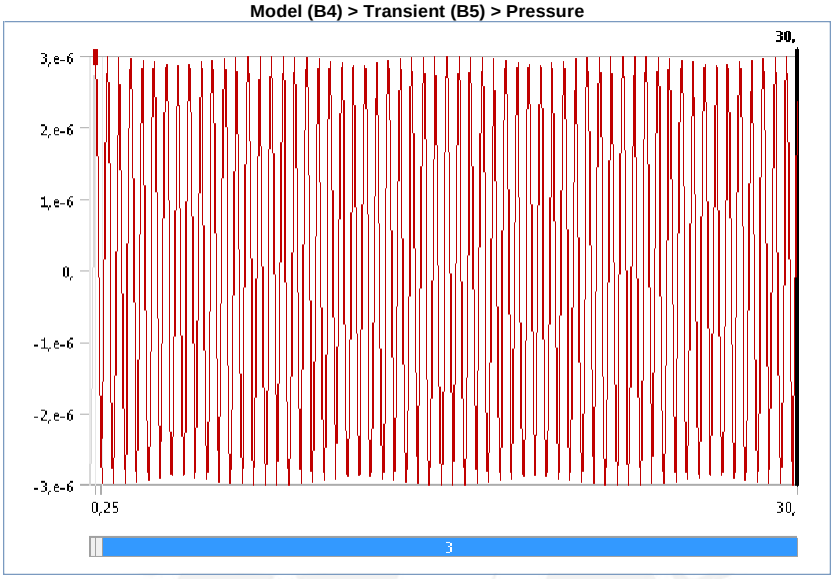

TABLE 19
Model (B4) > Transient (B5) > Command Snippet

Object Name	*Commands (APDL)*
State	Fully Defined
File	
File Name	D:\Benutzerdaten\StudentCesar\ANSYS_Model1_CSB\Principle_Range\Model1_CSB_Freq2.01\nerr.txt
File Status	All data current
Definition	
Suppressed	No
Step Selection Mode	All
Target	Mechanical APDL
Input Arguments	
ARG1	
ARG2	
ARG3	
ARG4	
ARG5	
ARG6	
ARG7	
ARG8	
ARG9	

Model (B4) > Transient (B5) > Commands (APDL)

```
!   Commands inserted into this file will be executed just prior to the ANSYS SOLVE command.
!   These commands may supersede command settings set by Workbench.

!   Active UNIT system in Workbench when this object was created: Metric (mm, kg, N, s, mV, mA)
!   NOTE: Any data that requires units (such as mass) is assumed to be in the consistent solver unit system.
!               See Solving Units in the help system for more information.

/NERR,,1e6,
```

Solution (B6)

TABLE 20
Model (B4) > Transient (B5) > Solution

Object Name	*Solution (B6)*
State	Solve Failed
Adaptive Mesh Refinement	
Max Refinement Loops	1,
Refinement Depth	2,
Information	
Status	Solve Required, Restart Available
Post Processing	

Calculate Beam Section Results	No

TABLE 21
Model (B4) > Transient (B5) > Solution (B6) > Solution Information

Object Name	*Solution Information*
State	Solve Failed
Solution Information	
Solution Output	Solver Output
Newton-Raphson Residuals	0
Update Interval	2,5 s
Display Points	All
FE Connection Visibility	
Activate Visibility	Yes
Display	All FE Connectors
Draw Connections Attached To	All Nodes
Line Color	Connection Type
Visible on Results	No
Line Thickness	Single
Display Type	Lines

TABLE 22
Model (B4) > Transient (B5) > Solution (B6) > Results

Object Name	*Y Axis - Directional Deformation - Selection - End Time*	*Y Axis - Directional Deformation - End Time*	*X Axis - Directional Deformation - Selection - End Time*
State	Solve Failed		
Scope			
Scoping Method	Named Selection	Geometry Selection	Named Selection
Named Selection	Selection		Selection
Geometry		All Bodies	
Definition			
Type	Directional Deformation		
Orientation	Y Axis		X Axis
By	Time		
Display Time	30, s	Last	
Coordinate System	Global Coordinate System		
Calculate Time History	Yes		
Identifier			
Suppressed	No		
Results			
Minimum	3,14 mm	-7,5123e-002 mm	-2,7803e-002 mm
Maximum	3,14 mm	1,1192 mm	-2,7803e-002 mm
Minimum Occurs On		Solid	
Maximum Occurs On		Line Body	
Minimum Value Over Time			
Minimum	-2,5115 mm		-0,25559 mm
Maximum	3,1545 mm	-1,5321e-007 mm	1,5386e-002 mm
Maximum Value Over Time			
Minimum	-2,5115 mm	6,7529e-007 mm	-0,25559 mm
Maximum	3,1545 mm		1,5386e-002 mm
Information			
Time	11,302 s	30, s	
Load Step	3		
Substep	5228	999999	
Iteration Number	51023	53522	

FIGURE 5
Model (B4) > Transient (B5) > Solution (B6) > Y Axis - Directional Deformation - Selection - End Time

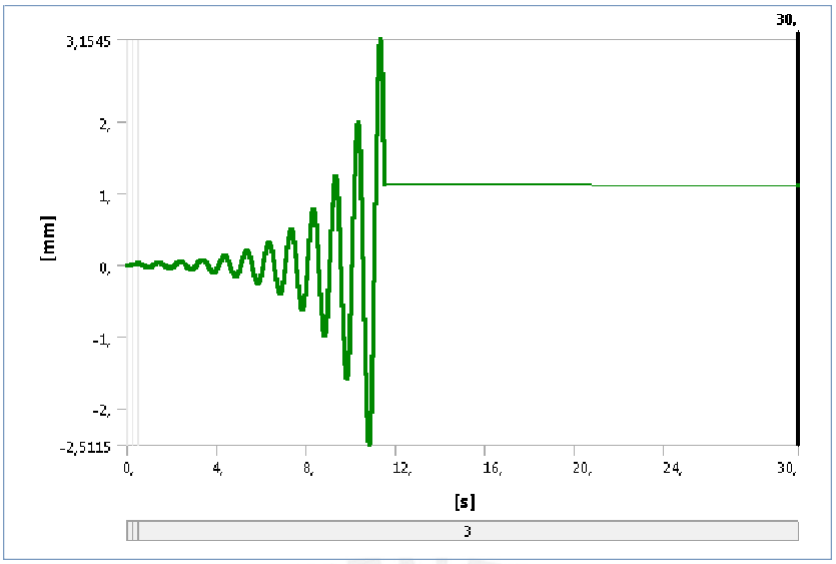

TABLE 23
Model (B4) > Transient (B5) > Solution (B6) > Y Axis - Directional Deformation - Selection - End Time

Time [s]	Minimum [mm]	Maximum [mm]
1,e-002	6,3553e-007	6,3553e-007
2,e-002	3,7996e-006	3,7996e-006
3,e-002	1,2008e-005	1,2008e-005
4,e-002	2,7955e-005	2,7955e-005
5,e-002	5,4999e-005	5,4999e-005
6,e-002	9,7326e-005	9,7326e-005
7,e-002	1,5917e-004	1,5917e-004
8,e-002	2,4411e-004	2,4411e-004
9,e-002	3,5527e-004	3,5527e-004
1,e-001	4,9561e-004	4,9561e-004
0,11	6,6754e-004	6,6754e-004
0,12	8,7294e-004	8,7294e-004
0,13	1,1131e-003	1,1131e-003
0,14	1,3892e-003	1,3892e-003
0,15	1,7031e-003	1,7031e-003
0,16	2,057e-003	2,057e-003
0,17	2,4535e-003	2,4535e-003
0,18	2,8948e-003	2,8948e-003
0,19	3,383e-003	3,383e-003
0,2	3,9203e-003	3,9203e-003
0,21	4,5084e-003	4,5084e-003
0,22	5,1479e-003	5,1479e-003
0,23	5,8386e-003	5,8386e-003
0,24	6,5798e-003	6,5798e-003
0,25	7,371e-003	7,371e-003
0,26	8,2114e-003	8,2114e-003
0,26641	8,7754e-003	8,7754e-003
0,27283	9,359e-003	9,359e-003
0,28244	1,0273e-002	1,0273e-002
0,29206	1,1234e-002	1,1234e-002
0,29806	1,1856e-002	1,1856e-002
0,30406	1,2492e-002	1,2492e-002
0,31307	1,3463e-002	1,3463e-002
0,32307	1,4548e-002	1,4548e-002
0,33248	1,5566e-002	1,5566e-002
0,34188	1,6578e-002	1,6578e-002
0,35129	1,7586e-002	1,7586e-002
0,36129	1,8654e-002	1,8654e-002
0,37129	1,9703e-002	1,9703e-002
0,38129	2,0711e-002	2,0711e-002
0,39129	2,1657e-002	2,1657e-002
0,40129	2,2532e-002	2,2532e-002
0,41128	2,3335e-002	2,3335e-002
0,42128	2,4076e-002	2,4076e-002
0,43057	2,4711e-002	2,4711e-002
0,43987	2,5274e-002	2,5274e-002
0,44987	2,5772e-002	2,5772e-002
0,45987	2,6139e-002	2,6139e-002
0,4662	2,6295e-002	2,6295e-002
0,47253	2,639e-002	2,639e-002

	-5,811e-002	-5,811e-002
11,467	-5,6026e-002	-5,6026e-002
11,468	-5,402e-002	-5,402e-002
11,469	-5,2084e-002	-5,2084e-002
11,47	-5,0223e-002	-5,0223e-002
11,471	-4,8446e-002	-4,8446e-002
11,472	-4,6751e-002	-4,6751e-002
11,473	-4,5184e-002	-4,5184e-002
11,474	-4,3774e-002	-4,3774e-002
11,475	-4,2521e-002	-4,2521e-002
11,476	-4,1454e-002	-4,1454e-002
11,477	-4,0551e-002	-4,0551e-002
11,478	-3,9736e-002	-3,9736e-002
11,479	-3,8951e-002	-3,8951e-002
11,48	-3,8159e-002	-3,8159e-002
11,481	-3,7347e-002	-3,7347e-002
11,482	-3,6533e-002	-3,6533e-002
11,483	-3,5726e-002	-3,5726e-002
11,484	-3,4928e-002	-3,4928e-002
11,485	-3,4162e-002	-3,4162e-002
11,486	-3,3441e-002	-3,3441e-002
11,487	-3,2745e-002	-3,2745e-002
11,488	-3,2059e-002	-3,2059e-002
11,489	-3,1381e-002	-3,1381e-002
11,49	-3,0728e-002	-3,0728e-002
11,491	-3,0126e-002	-3,0126e-002
11,492	-2,955e-002	-2,955e-002
11,493	-2,8959e-002	-2,8959e-002
11,494	-2,8366e-002	-2,8366e-002
30,	-2,7803e-002	-2,7803e-002

Material Data

Material_Beam

TABLE 26
Material_Beam > Constants

Density	1,e-006 kg mm^-3

TABLE 27
Material_Beam > Isotropic Elasticity

Temperature C	Young's Modulus MPa	Poisson's Ratio	Bulk Modulus MPa	Shear Modulus MPa
	1,0313e-002	0,	3,4377e-003	5,1565e-003

Material_Null

TABLE 28
Material_Null > Constants

Density	1,e-015 kg mm^-3

TABLE 29
Material_Null > Isotropic Elasticity

Temperature C	Young's Modulus MPa	Poisson's Ratio	Bulk Modulus MPa	Shear Modulus MPa
	2,e+007	0,	6,6667e+006	1,e+007